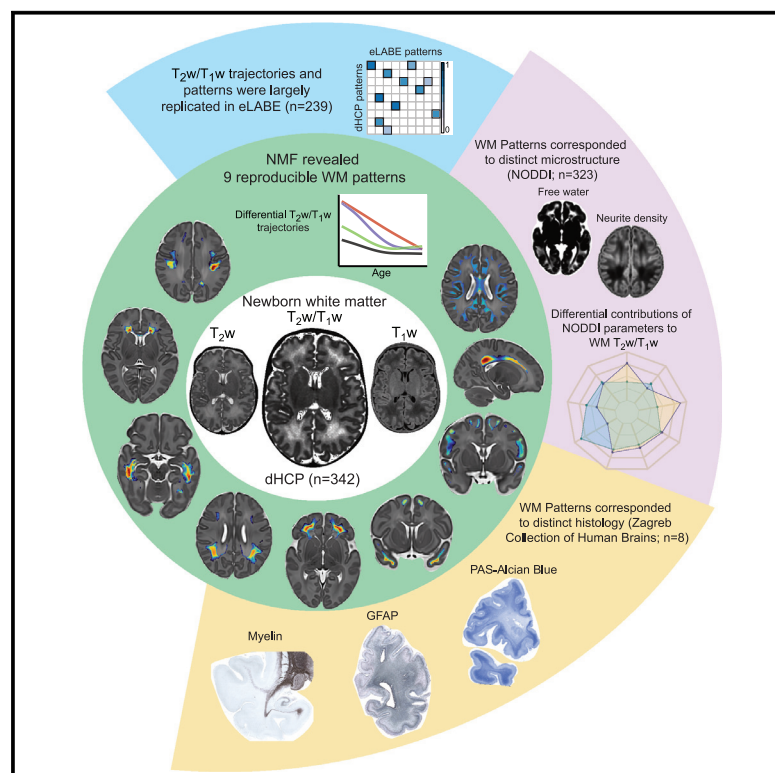


# Neurodevelopmental patterns of early postnatal white matter maturation represent distinct underlying microstructure and histology

## Graphical abstract



## Authors

Arash Nazari, Željka Krsnik, Ivica Kostović, ..., Jeffrey J. Neil, Christopher D. Smyser, Aristeidis Sotiras

## Correspondence

a.nazari@wustl.edu (A.N.),  
aristeidis.sotiras@wustl.edu (A.S.)

## In brief

Using high-resolution  $T_2$ -/ $T_1$ -weighted MR images from a large sample, Nazari et al. identify reproducible patterns of coordinated white matter maturation during the early postnatal period that correspond to distinct developmental trajectories, microstructure, and histology. These results provide important context for understanding the complexities of white matter development in health and disease.

## Highlights

- Analysis of postnatal WM  $T_2w/T_1w$  signal reveals coordinated maturational patterns
- WM maturational patterns show differential developmental trajectories
- These maturational patterns correspond to distinct WM microstructure and histology

Article

# Neurodevelopmental patterns of early postnatal white matter maturation represent distinct underlying microstructure and histology

Arash Nazeri,<sup>1,\*</sup> Željka Krsnik,<sup>2</sup> Ivica Kostović,<sup>2</sup> Sung Min Ha,<sup>1</sup> Janja Kopic,<sup>2</sup> Dimitrios Alexopoulos,<sup>3</sup> Sydney Kaplan,<sup>3</sup> Dominique Meyer,<sup>3</sup> Joan L. Luby,<sup>4</sup> Barbara B. Warner,<sup>5</sup> Cynthia E. Rogers,<sup>4</sup> Deanna M. Barch,<sup>1,4,6</sup> Joshua S. Shimony,<sup>1</sup> Robert C. McKinstry,<sup>1</sup> Jeffrey J. Neil,<sup>3</sup> Christopher D. Smyser,<sup>1,3,5</sup> and Aristeidis Sotiras<sup>1,7,8,\*</sup>

<sup>1</sup>Mallinckrodt Institute of Radiology, Washington University School of Medicine, Saint Louis, MO 63110, USA

<sup>2</sup>Croatian Institute for Brain Research, School of Medicine, University of Zagreb School of Medicine, Zagreb 10000, Croatia

<sup>3</sup>Department of Neurology, Washington University School of Medicine, Saint Louis, MO 63110, USA

<sup>4</sup>Department of Psychiatry, Washington University School of Medicine, Saint Louis, MO 63110, USA

<sup>5</sup>Department of Pediatrics, Washington University School of Medicine, Saint Louis, MO 63110, USA

<sup>6</sup>Psychological & Brain Sciences, Washington University School in St. Louis, Saint Louis, MO 63130, USA

<sup>7</sup>Institute for Informatics, Washington University School of Medicine, Saint Louis, MO 63108, USA

<sup>8</sup>Lead contact

\*Correspondence: [a.nazeri@wustl.edu](mailto:a.nazeri@wustl.edu) (A.N.), [aristeidis.sotiras@wustl.edu](mailto:aristeidis.sotiras@wustl.edu) (A.S.)

<https://doi.org/10.1016/j.neuron.2022.09.020>

## SUMMARY

Cerebral white matter undergoes a rapid and complex maturation during the early postnatal period. Prior magnetic resonance imaging (MRI) studies of early postnatal development have often been limited by small sample size, single-modality imaging, and univariate analytics. Here, we applied nonnegative matrix factorization, an unsupervised multivariate pattern analysis technique, to  $T_2w/T_1w$  signal ratio maps from the Developing Human Connectome Project ( $n = 342$  newborns) revealing patterns of coordinated white matter maturation. These patterns showed divergent age-related maturational trajectories, which were replicated in another independent cohort ( $n = 239$ ). Furthermore, we showed that  $T_2w/T_1w$  signal variations in these maturational patterns are explained by differential contributions of white matter microstructural indices derived from diffusion-weighted MRI. Finally, we demonstrated how white matter maturation patterns relate to distinct histological features by comparing our findings with postmortem late fetal/early postnatal brain tissue staining. Together, these results delineate concise and effective representation of early postnatal white matter reorganization.

## INTRODUCTION

The late fetal/early postnatal period is a critical stage of human brain development, during which the cerebral white matter undergoes complex changes (Barkovich and Barkovich, 2019; Gilmore et al., 2018; Vasung et al., 2019). These processes are characterized by myelination of the major white matter bundles, maturation of the extracellular matrix, continuation of neural migration, and continued dissolution of the transient laminar organization of the fetal period, including disappearance of the subplate zone at the white matter-cortex interface (Barkovich and Barkovich, 2019; Kinney and Volpe, 2018; Kostović et al., 2014; Paredes et al., 2016). However, early postnatal white matter maturation may be disrupted by preterm birth, interrupting normal fetal brain development (Mathur et al., 2010; Volpe, 2009), or altered by other environmental or genetic factors, leading to neurological and psychiatric disorders later in life (Guma et al., 2019; Hazlett et al., 2017; Marín, 2016). Thus, identifying

patterns of typical white matter development during this period is critical for accounts of both healthy brain maturation and advancing understanding of neurodevelopmental disorders.

A growing number of studies have investigated white matter maturation using high quality magnetic resonance imaging (MRI) in newborns. Volumetric studies have demonstrated a steep white matter volume expansion in the early postnatal period and relatively decreased white matter volumes in preterm infants (Alexander et al., 2019; Makropoulos et al., 2016). Diffusion tensor imaging (DTI) studies have further revealed substantive changes in white matter microstructure during this period, including decreases in white matter diffusivity and increases in fractional anisotropy (Dean et al., 2017; Dubois et al., 2014; Gilmore et al., 2007; Mukherjee et al., 2001, 2002), along with altered diffusion metrics in preterm infants (Brenner et al., 2021; Knight et al., 2018). Additionally, the evolution of MRI signal on  $T_2$ -weighted ( $T_2w$ ) and  $T_1$ -weighted ( $T_1w$ ) images has been used to track early postnatal white matter microstructural

changes, such as myelination and extracellular matrix maturation (Corbett-Detig et al., 2011; Kostović et al., 2002; Kostović et al., 2014; O'Muircheartaigh et al., 2020; Paredes et al., 2016; Pittet et al., 2019; Wang et al., 2019; Widjaja et al., 2010; Žunić Išasegi et al., 2018).

Although these MRI studies have improved our understanding of early postnatal white matter development, most have relied on single-modality data despite the importance of cross-examining findings with other neuroimaging modalities and brain histology to better elucidate the underlying mechanisms. Convergent results from different modalities can ensure the validity of the findings and minimize the effects of modality-specific biases (Eickhoff et al., 2018). Moreover, while white matter maturational processes tend to occur in radially organized periventricular, intermediate, and superficial white matter compartments (Kostović et al., 2014; Pittet et al., 2019), many studies have focused on white matter tracts (Dean et al., 2017; Gilmore et al., 2007). Therefore, tract-based approaches may not be able to fully capture the compartmental maturation of the white matter. Additionally, region-of-interest approaches (Kunz et al., 2014) are limited by the *a priori* selection of regions, which restricts their ability to identify and characterize diffuse developmental processes that occur across multiple brain areas. Finally, past accounts have frequently been limited by small sample sizes and analytics that do not evaluate complex multivariate imaging patterns.

To overcome these previous limitations, we capitalized on a large sample of newborns studied through the Developing Human Connectome Project (dHCP) (Makropoulos et al., 2018). We used high-resolution MR acquisitions to calculate  $T_2w/T_1w$  signal intensity ratio maps. This allowed us to enhance the contrast-to-noise ratio (Glasser and Van Essen, 2011; Lee et al., 2015) and better characterize critical postnatal cerebral white matter developmental processes, which result in opposing effects on  $T_1w$  and  $T_2w$  signal intensity (decreased intensity on  $T_2w$  and increased intensity on  $T_1w$  images) (Corbett-Detig et al., 2011; Kostović et al., 2002, 2014; O'Muircheartaigh et al., 2020; Paredes et al., 2016; Pittet et al., 2019; Wang et al., 2019; Widjaja et al., 2010; Žunić Išasegi et al., 2018). We further leveraged advances in unsupervised multivariate pattern analysis to analyze white matter  $T_2w/T_1w$  ratio maps. Specifically, we delineated spatial patterns of cerebral white matter maturation using nonnegative matrix factorization (NMF), which provides a parts-based representation of complex high dimensional datasets (Brunet et al., 2004; Lee and Seung, 1999; Wu et al., 2016) and has recently been adapted for neuroimaging data (Sotiras et al., 2015, 2017).

We hypothesized that early postnatal cerebral white matter changes occur in concert with distinct spatial patterns that follow laminar compartmental white matter reorganization. Given the complexity and regional variations of the early postnatal white matter maturation, we further predicted that these spatial patterns would show distinct age trajectories of MRI signal evolution, exhibit different susceptibilities to preterm birth, and represent distinct underlying white matter microstructure and histology. As hypothesized, the NMF-derived set of coordinated white matter maturation patterns exhibited a radially distributed compartmental organization with respect to the lateral ventricles and the cortical ribbon, showed distinct maturational trajectories

and vulnerabilities to preterm birth, and were largely robust to different image processing parameters. We further replicated the differential age-related rate of decline in  $T_2w/T_1w$  signal in the identified white matter patterns in an independent large imaging cohort of newborns, part of the Early Life Adversity, Biological Embedding, and Risk for Developmental Precursors of Mental Disorders (eLABLE) study. Additionally, similar patterns of white matter maturation re-emerged when NMF was applied to the  $T_2w/T_1w$  signal ratio maps from the eLABLE study. We used neurite orientation dispersion and density imaging (NODDI) modeling of diffusion-weighted MRI (Zhang et al., 2012a), aiming to disentangle the tissue microstructural determinants of the early postnatal white matter signal maturation. We observed that changes in NODDI-derived white matter free water content and neurite density differentially contribute to patterns of  $T_2w/T_1w$  signal changes. Finally, we compared our findings with postmortem late fetal/early postnatal brain specimens from the Zagreb Collection of Human Brains (Hrabáč et al., 2018) and showed how white matter maturation patterns relate to distinct histological features.

## RESULTS

### Description of dHCP and eLABLE participants

After quality control of neuroimaging data,  $T_2w$  and  $T_1w$  images from 342 newborns from the dHCP cohort were included in the main study (age at scan: 35–45 weeks postmenstrual, Table S1; see [method details](#) for further details). Of the 72 preterm-born infants in the dHCP data (born before 37-weeks' gestation), 39 underwent MRI at term-equivalent age or older (i.e., at the time that they reached 37 weeks postmenstrual age or later). Quality-controlled MRI data from the eLABLE cohort ( $n = 239$ ; age at scan: 38–44 weeks postmenstrual, Table S1; see [method details](#) for further details) were used for replication, which included data from 38 preterm-born infants. Of note, all participants in the eLABLE study were imaged at term-equivalent age or older.

### Postmenstrual age and prematurity strongly impact cerebral white matter $T_2w/T_1w$ signal ratio

We first sought to investigate whether the white matter  $T_2w/T_1w$  ratio is a sensitive marker for early postnatal cerebral white matter development. Accordingly, we examined the association of mean cerebral white matter  $T_2w/T_1w$  with postmenstrual age and prematurity using generalized additive models (GAMs). Results revealed that mean white matter  $T_2w/T_1w$  was associated with age and preterm birth in the dHCP cohort. Specifically, mean white matter  $T_2w/T_1w$  values nonlinearly decreased with age ( $R^2 = 0.30$ ; effective degrees of freedom [edf] = 2.85;  $p < 2 \times 10^{-16}$ , Figure 1). There was no significant sex effect or sex-by-age interaction effect on mean white matter  $T_2w/T_1w$  ratio. Among the term-equivalent or older infants ( $n_{\text{Term}} = 270$ ,  $n_{\text{Preterm}} = 39$ ), preterm birth was associated with a higher mean white matter  $T_2w/T_1w$  signal ratio (adjusted for postmenstrual age:  $t = -8.5$ ,  $p = 5.4 \times 10^{-16}$ ; Figure 1). Next, we repeated these analyses in the eLABLE cohort, obtaining consistent results. We observed a significant linear age-related decline in mean white matter  $T_2w/T_1w$  signal ratio ( $R^2 = 0.22$ ,  $\text{edf} = 1$ ,  $p = 9.3 \times 10^{-15}$ ) and a trend toward a higher  $T_2w/T_1w$  signal ratio in preterm newborns (adjusted for

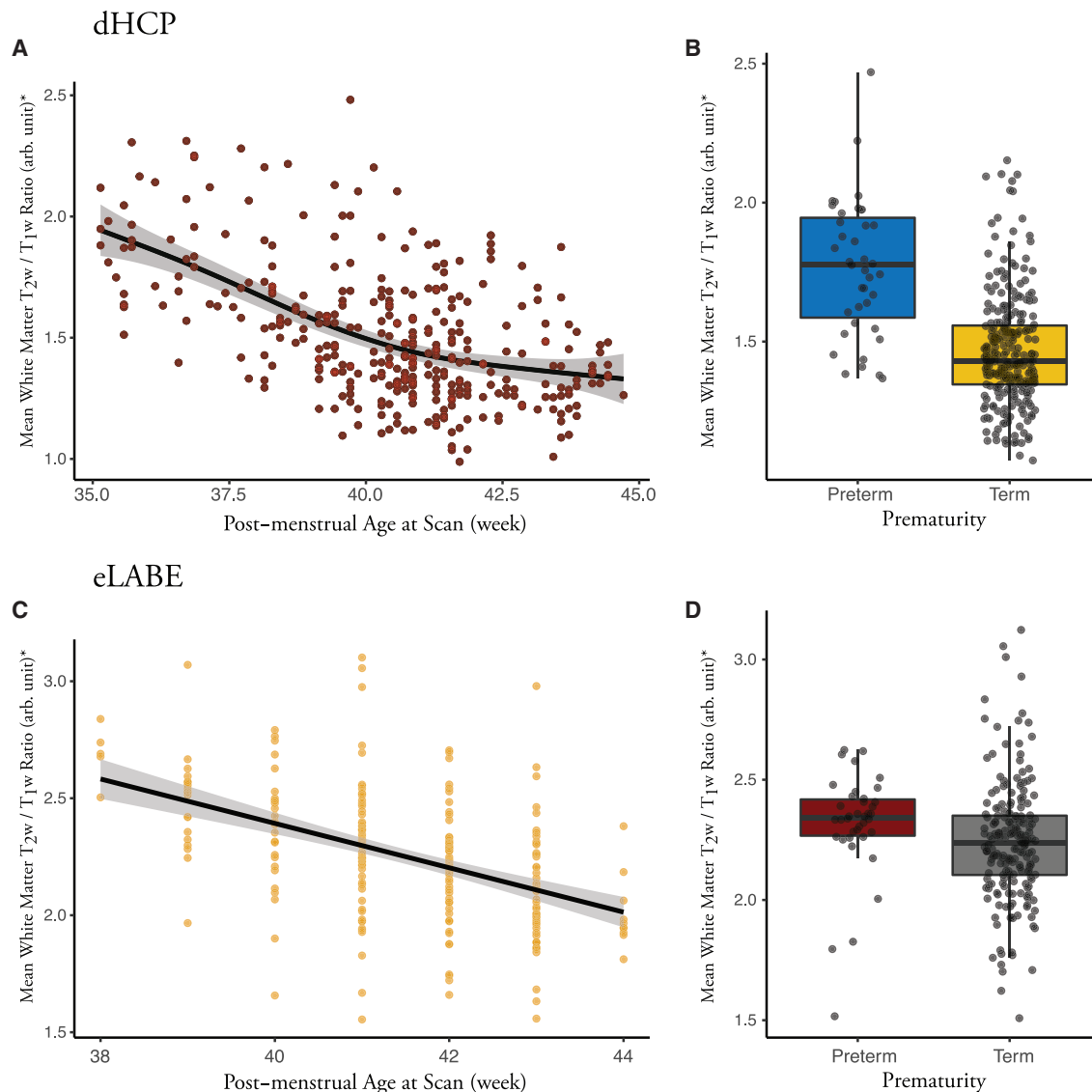


**Figure 1. Effects of age and preterm birth on mean cerebral white matter  $T_{2w}/T_{1w}$  signal intensity ratio**

(A) Nonlinear decrease in white matter  $T_{2w}/T_{1w}$  signal intensity ratio with age in the dHCP cohort.

(B) Effect of preterm birth on white matter  $T_{2w}/T_{1w}$  signal intensity ratio in the dHCP cohort.

(C) Decrease in mean white matter  $T_{2w}/T_{1w}$  signal intensity ratio with age in the eLABE cohort. A linear model was fitted, given that most of the subjects in the eLABE cohort fell into a narrower range of age (39–43 weeks postmenstrual age).

(D) Effect of preterm birth on white matter  $T_{2w}/T_{1w}$  signal intensity ratio in the eLABE cohort.

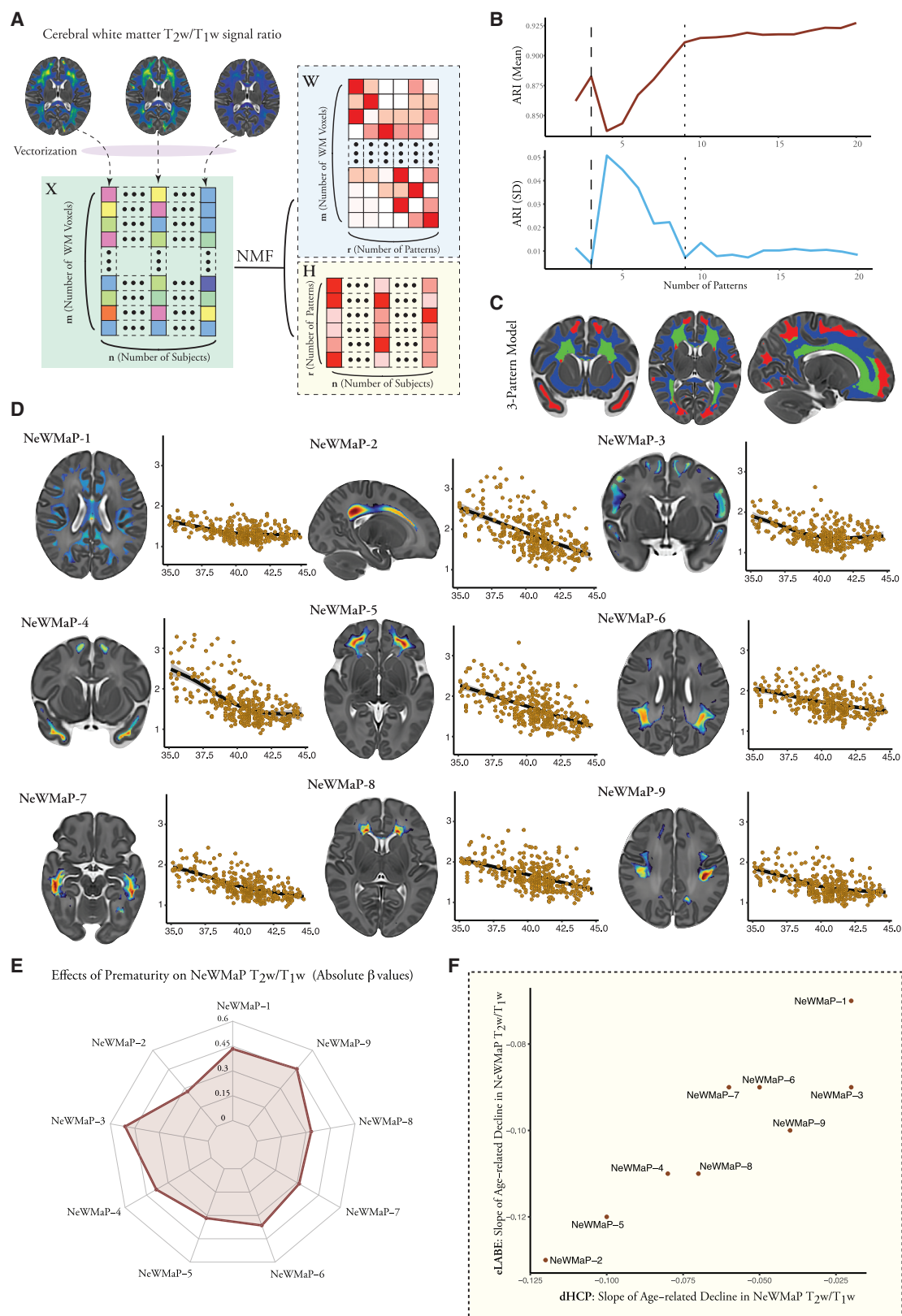
Error bands represent 95% confidence intervals (A,C). Boxplot center lines represent median; the lower and upper hinges correspond to the 25th and 75th percentiles; the lower/upper whisker extends from the hinge to the smallest/largest value no further than  $1.5 \times$  inter-quartile range (B,D).

\*Age-adjusted mean white matter  $T_{2w}/T_{1w}$  signal intensity ratio values.

postmenstrual age:  $t = -1.8$ ,  $p = 0.06$ ;  $n_{\text{Term}} = 201$ ,  $n_{\text{Preterm}} = 38$ ). The absence of images from younger newborns (<38 weeks postmenstrual) in the eLABE study limited the ability to identify nonlinear age effects in this cohort. Moreover, the weaker effect observed for prematurity in the eLABE study likely stems from the older gestational age at birth among its preterm newborns (mean [standard deviation, SD] postmenstrual age of preterm newborns in eLABE = 34.3 [2.2] weeks versus dHCP = 31.5 [3.6] weeks;  $p = 8.2 \times 10^{-5}$ ).

### NMF identifies reproducible and hierarchical early postnatal white matter developmental patterns

We next sought to investigate whether cerebral white matter matures through the development of spatially heterogeneous yet regionally coordinated patterns (Figure 2). To this end, we applied NMF to the white matter  $T_{2w}/T_{1w}$  ratio maps from the dHCP cohort. To identify the most reproducible and reliable solution with the least reconstruction error, we examined multiple NMF solutions ranging from  $K = 2$  to 20 patterns. Overall, NMF



(legend on next page)

solutions across different resolutions demonstrated high similarity in parcellation of the cerebral white matter (Figure S1A), suggesting hierarchical partitioning of the coarser patterns into finer subdivisions at higher resolutions.

Split-half reproducibility analysis, as quantified using the adjusted rand index (ARI) (Hubert and Arabie, 1985), demonstrated that solutions were highly stable, emphasizing the robustness of the identified patterns. However, reproducibility and reliability were not uniform. Reproducibility (i.e., high mean ARI across bootstraps) peaked at the 3-pattern solution (mean ARI: 88.2%) and then reached a relative plateau after the 9-pattern solution (mean ARI: 91.1%). The highest reliability (i.e., high stability with low ARI, SD across bootstraps) occurred for the 3-pattern (SD = 0.5%) and 9-pattern (SD = 0.7%) solutions. Hence, 3-pattern and 9-pattern solutions were further explored as the simplest solutions with high reproducibility and reliability (Figure 2B).

The 3-pattern solution distinguished patterns by largely following distance from the lateral ventricles. The first pattern comprised periventricular white matter, which further extended into the deep white matter of the frontal and parietal lobes. The second pattern consisted of frontotemporal polar superficial white matter, while the remaining superficial and deep white matter areas formed the third pattern (Figure 2C).

These three patterns were further divided hierarchically as part of the 9-pattern NMF solution (Figure 2D; Table S2). Given that the 9-pattern solution demonstrated a lower reconstruction error than the 3-pattern model (Figure S1B), the nine newborn white matter maturation patterns (NeWMaPs) were used for downstream analyses. Despite being derived in a completely unsupervised and data-driven manner, NeWMaPs were remarkably symmetric and demonstrated a characteristic distance distribution with respect to the cortex and/or the lateral ventricles (Figure S2B; Table S2). Three NeWMaPs localized mainly to the superficial white matter: (1) NeWMaP-1, predominantly sulcal aspects of the superficial white matter throughout the brain in addition to major white matter bundles (e.g., corpus callosum, cingula, and external capsules); (2) NeWMaP-4, superficial white matter in the temporal poles, frontal poles/superior frontal gyri, precune, and occipital poles; and (3) NeWMaP-3, all other gyral

superficial white matter areas. Three other NeWMaPs corresponded to the periventricular white matter: (1) NeWMaP-2, dorsal frontoparietal periventricular region and centrum semiovale; (2) NeWMaP-7, occipitotemporal periventricular region; and (3) NeWMaP-8, corpus callosum genu/forceps minor and frontal periventricular region. The last three NeWMaPs were intermediate in distance to the cortex and lateral ventricles: (1) NeWMaP-5, rostral/orbital frontal intermediate region; (2) NeWMaP-6, posterior parietal superior longitudinal fasciculus, and parietal and dorsal frontal intermediate region; and (3) NeWMaP-9, superior longitudinal fasciculus, perirolandic white matter surrounding the central sulci and occipital poles.

Similar white matter maturation patterns re-emerged with alternative registration and preprocessing approaches: (1) registration to previously generated neonatal brain templates without the use of distance maps (to the ventricle/cortex) (Figure S1C) and (2) without smoothing of  $T_2w/T_1w$  signal ratio maps (Figure S1D). Notably, NeWMaP-8 was not replicated with these alternative approaches, which could suggest the sensitivity of this small pattern to registration inaccuracies and differences in preprocessing due to its intricate internal structure (Figure S2C).

### NeWMaPs display differential developmental effects

The data-driven NMF approach identified patterns of covariance in this large developmental sample but did not include information regarding participant postmenstrual age or prematurity. Accordingly, we next investigated the developmental patterns across NeWMaPs using GAMs. Although all NeWMaPs demonstrated a significant age-related decline in mean  $T_2w/T_1w$  signal ratio, their trajectories displayed substantial heterogeneity. The steepest decline was observed in the dorsal frontoparietal periventricular NeWMaP-2, and the lowest rate of decline was in the predominantly sulcal superficial NeWMaP-1 (Figure 2D; Table S3). After correcting for multiple comparisons, there was no significant sex effect or sex-by-age interaction effect on NeWMaP  $T_2w/T_1w$  signal ratios (Table S4). These age trajectories were not significantly affected by head circumference or mean absolute motion (derived from diffusion-weighted MRI motion correction as a proxy measure for in-scanner motion; Table S4).  $T_2w/T_1w$  signal ratio extracted from NeWMaP-7,

### Figure 2. Nonnegative matrix factorization (NMF) of $T_2w/T_1w$ ratio maps

(A) An overview of  $T_2w/T_1w$  ratio image data NMF. Three-dimensional cerebral white matter  $T_2w/T_1w$  ratio maps are initially vectorized and then concatenated into matrix **X** (each column representing a subject; each row representing a voxel in the template space). NMF then decomposes the matrix **X** into: (i) matrix **W**: the factor representations (each column representing a factor; each row representing a white matter voxel in the template space); (ii) matrix **H**: the subject-specific loading coefficients for each factor (each column representing a subject; each row representing a factor).

(B) Split-half reproducibility analysis with bootstrapping of NMF solutions at multiple resolutions ranging from 2 to 20 white matter factors (mean and standard deviation of adjusted rand index [ARI] over 10 bootstrap resamples). Although mean ARI peaks at 9-factor solution and then plateaus at 9-factor NMF solution, two clear dips in standard deviation of the ARI across bootstraps can be observed at 3 and 9 NMF components. F-tests show that the variation of ARI across bootstraps was significantly lower at 3-factor solution compared with 2-factor ( $F_{9,9} = 5.98$ ,  $P_{one-tailed} = 0.0068$ ) and 4-factor solutions ( $F_{9,9} = 119.9$ ,  $P_{one-tailed} = 2.75 \times 10^{-8}$ ). Similarly, variation of ARI across bootstraps was significantly lower at 9-factor solution compared with 8-factor ( $F_{9,9} = 9.52$ ,  $P_{one-tailed} = 0.0013$ ) and 10-factor solutions ( $F_{9,9} = 3.47$ ,  $P_{one-tailed} = 0.039$ ).

(C) Visualization of the NeWMaPs from the three-factor NMF model.

(D) Visualization of the NeWMaPs from the nine-factor NMF model (see also Figure S2A) and corresponding age-related changes in mean  $T_2w/T_1w$  signal ratio in these NeWMaPs. NeWMaP-2, NeWMaP-5, and NeWMaP-4 showed the highest early postnatal  $T_2w/T_1w$  values, while NeWMaP-1 and NeWMaP-9 showed the lowest early postnatal  $T_2w/T_1w$  values. Color maps indicate relative loadings for each NeWMaP with warmer colors corresponding to higher values (X-rain colormap is used). Error bands represent 95% confidence intervals.

(E) Effects of prematurity on NeWMaP  $T_2w/T_1w$  signal ratio in term-equivalent or older newborns.

(F) Age-related decline rates of NeWMaP  $T_2w/T_1w$  signal ratio in the eLAbE study and a comparable subset of the dHCP newborns (linear models; postmenstrual age  $\geq 38$  weeks, Table S1).

NeWMaP-4, and NeWMaP-2 showed the smallest errors in predicting newborn age (Table S5).

Among term-equivalent newborns, preterm birth was associated with a higher mean  $T_2w/T_1w$  signal ratio in all NeWMaPs, with the strongest effect on superficial NeWMaP-3, followed by the periorlandic intermediate NeWMaP-9, and sulcal superficial NeWMaP-1 (Figures 2E and S3). Moreover, all three periventricular and two of the intermediate NeWMaPs showed a less steep rate of decline in  $T_2w/T_1w$  signal ratio in premature newborns (age  $\times$  prematurity interaction effects with nominal  $p < 0.05$ : NeWMaP-2:  $p = 0.028$ ; NeWMaP-5:  $p = 0.014$ ; NeWMaP-6:  $p = 0.028$ ; NeWMaP-7:  $p = 0.025$ ; NeWMaP-8:  $p = 0.0021$ ).

### Replication of NeWMaPs in the independent eLAbE newborn imaging data

To determine whether similar age trajectories would be found in an independent study, we used the NeWMaPs derived from the dHCP cohort as regions of interest to extract mean  $T_2w/T_1w$  signal ratios in the eLAbE study. Similar to dHCP results, all NeWMaPs demonstrated a significant age-related decline in  $T_2w/T_1w$  signal ratio (Figure S4). To directly compare dHCP and eLAbE results, we calculated the correlation between the rates of age-related decline in  $T_2w/T_1w$  signal ratio across all NeWMaPs. To eliminate the effect of postmenstrual age differences between the two studies, the correlation was calculated between the eLAbE sample (all postmenstrual ages are  $\geq 38$  weeks) and a subset of dHCP newborns ( $n = 296$ , Table S1), which was obtained by excluding participants with postmenstrual age at scan  $< 38$  weeks. We found a high correlation between the rates of age-related decline in  $T_2w/T_1w$  signal ratio of the NeWMaPs in the dHCP and eLAbE studies (Figure 2F, Spearman  $\rho$ : 0.92,  $p = 0.001$ ).

In addition, to demonstrate the replicability of our approach in deriving patterns of early postnatal white matter patterns in an independent dataset, we applied NMF to  $T_2w/T_1w$  signal ratio maps from the eLAbE dataset (with a 9-factor solution). We then used cosine similarity (range 0–1; higher values indicate greater similarity) to compare the resulting factors from the eLAbE dataset with the dHCP NeWMaPs. The similarity matrix between dHCP NeWMaPs and factors driven from the eLAbE dataset illustrates that a great majority of dHCP NeWMaPs re-emerged in the eLAbE dataset (Figure 3A). Apart from NeWMaP-3 and NeWMaP-9, dHCP NeWMaPs showed a relatively high overlap with a single eLAbE NMF factor (cosine similarity  $\geq 0.6$ ; Figure 3B). Both intermediate (NeWMaP-5) and periventricular (NeWMaP-8) rostral frontal dHCP NeWMaPs showed high overlap with a single eLAbE factor. Similarly, the intermediate (NeWMaP-2) and periventricular (NeWMaP-9) frontoparietal dHCP NeWMaPs were represented by the same eLAbE factor (Figure 3C). Superficial white matter NeWMaP-3 corresponded to two eLAbE factors (Figure 3D).

### Free water content and neurite density differentially contribute to NeWMaP $T_2w/T_1w$ signal ratio

Given the heterogeneity in  $T_2w/T_1w$  signal ratio across the NeWMaPs, we hypothesized that distinct white matter tissue microstructural properties contribute to the observed signal changes during early postnatal white matter maturation. Hence, we investigated whether neurodevelopmental patterns derived

from  $T_2w/T_1w$  signal ratio are linked to differences in tissue microstructure indices derived independently from diffusion-weighted MRI. To this end, we fitted the NODDI model to the available multi-shell diffusion MR images in the dHCP dataset (Zhang et al., 2012a) ( $n = 323$ , Table S1). Unlike DTI, the NODDI model can disentangle compartmental diffusion properties in complex tissue microenvironments, such as early postnatal white matter (Zhang et al., 2012b). Capitalizing on this property, we estimated tissue compartments and generated free water, neurite density, and orientation dispersion maps. We additionally generated weekly average NODDI parameter maps in the template space (made publicly available at Zenodo: <https://doi.org/10.5281/zenodo.6782004>). This allowed us to visually compare the spatiotemporal patterns of microstructural variations with respect to NeWMaPs. The NeWMaPs were well-demarcated on free water and/or NDI maps (Figure 4A). Furthermore, the application of NeWMaP masks to the weekly average NODDI parameter maps revealed that NeWMaPs largely corresponded to distinct distributions of white matter free water and neurite density (Figure S5).

To further investigate links between white matter  $T_2w/T_1w$  signal ratio and diffusion-derived tissue microstructure indices, we applied NeWMaP masks to individual free water, neurite density, and orientation dispersion maps. This allowed us to quantify the mean value for each of these indices within each NeWMaP at the individual level. We used the derived measures as explanatory variables in linear models that predict mean  $T_2w/T_1w$  signal ratio to assess the respective contributions of white matter microstructure indices to the  $T_2w/T_1w$  signal ratio in each NeWMaP. Higher free water content was associated with a higher  $T_2w/T_1w$  signal ratio, while higher neurite density was associated with a lower  $T_2w/T_1w$  signal ratio in all NeWMaPs. Higher orientation dispersion was associated with a higher  $T_2w/T_1w$  signal ratio in some NeWMaPs (mainly among the NeWMaPs with higher neurite density contributions). Across all NeWMaPs, NODDI indices together explained the majority of white matter  $T_2w/T_1w$  signal ratio variance ( $R^2$ : 0.50–0.85, Table S6). However, the degree of contribution from each tissue microstructure index was different. Although neurite density showed a dominant effect on rostral frontal periventricular NeWMaP-8 and sulcal superficial NeWMaP-1  $T_2w/T_1w$  signal ratio, free water had a dominant effect on the gyral superficial NeWMaP-3 and NeWMaP-4  $T_2w/T_1w$  signal ratio (Figure 4B; Table S6). Free water content significantly decreased with age (Figure 4C), while neurite density increased with age across all NeWMaPs (Figure 4D). Similarly, prematurity was associated with significantly higher free water content (except for NeWMaP-5) and lower neurite density in all NeWMaPs (except for NeWMaP-7 and NeWMaP-8; Table S7). These results, together with the heterogeneity of developmental effects, suggest that different NeWMaPs may be linked in part to distinct neurodevelopmental and histological processes, which we examined next.

### NeWMaPs correspond to late fetal/early postnatal histological reorganization

The hallmarks of late fetal/early postnatal white matter development are myelination, maturation of the astroglial arrangements,

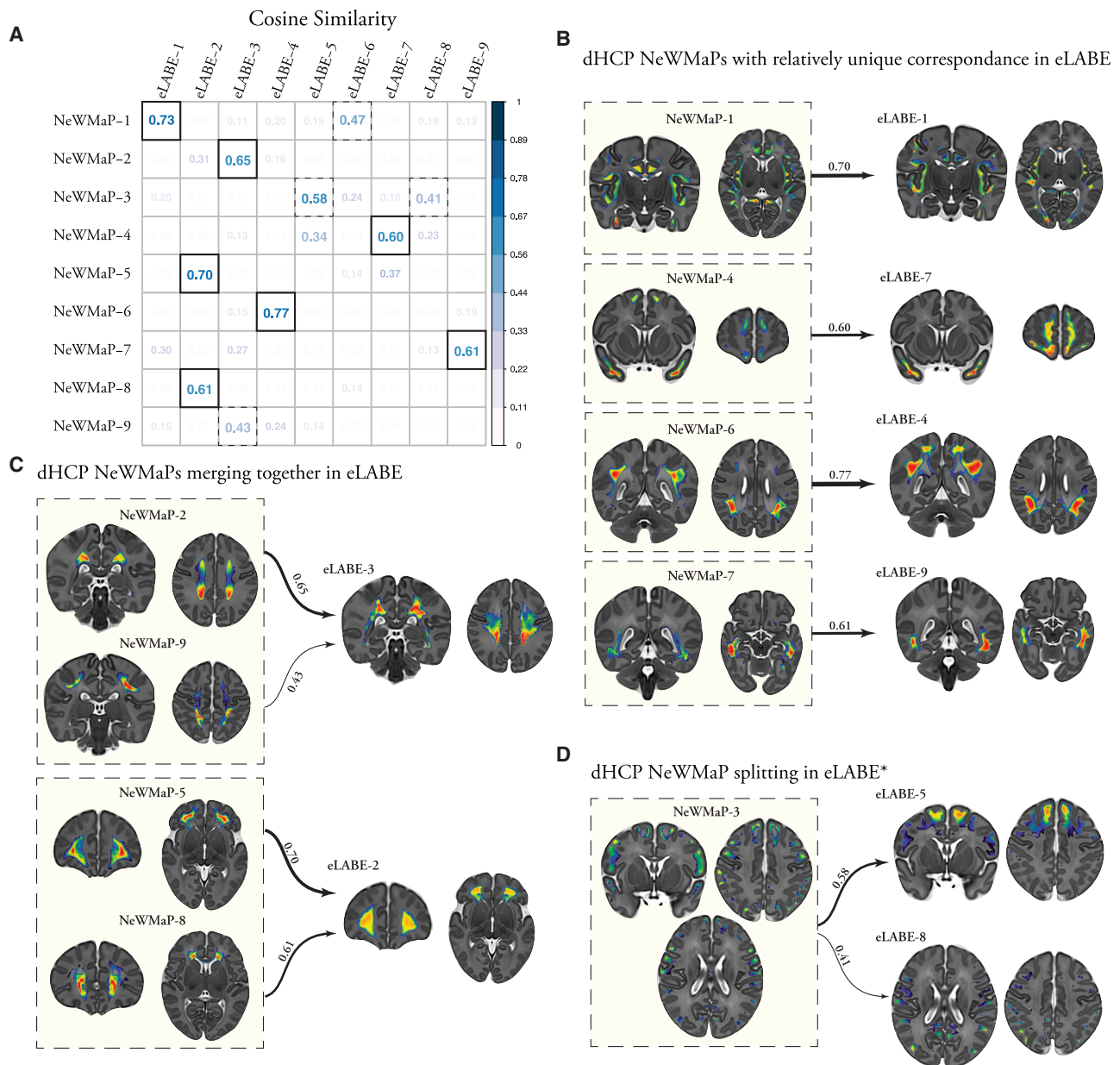


**Figure 3. Re-emergence of similar early postnatal white matter maturation patterns in the eLAbE study**

(A) Similarity matrix (cosine similarity; ranging from 0 to 1) between dHCP NeWMaPs and NMFs derived from eLAbE. Except for NeWMaP-3 and NeWMaP-9, all NeWMaPs showed high overlap with a single eLAbE factor (cosine similarity  $\geq 0.6$ ; solid boxes). Moderate overlaps are demarcated by dashed lines (cosine similarity  $\geq 0.4$  and  $< 0.6$ ).

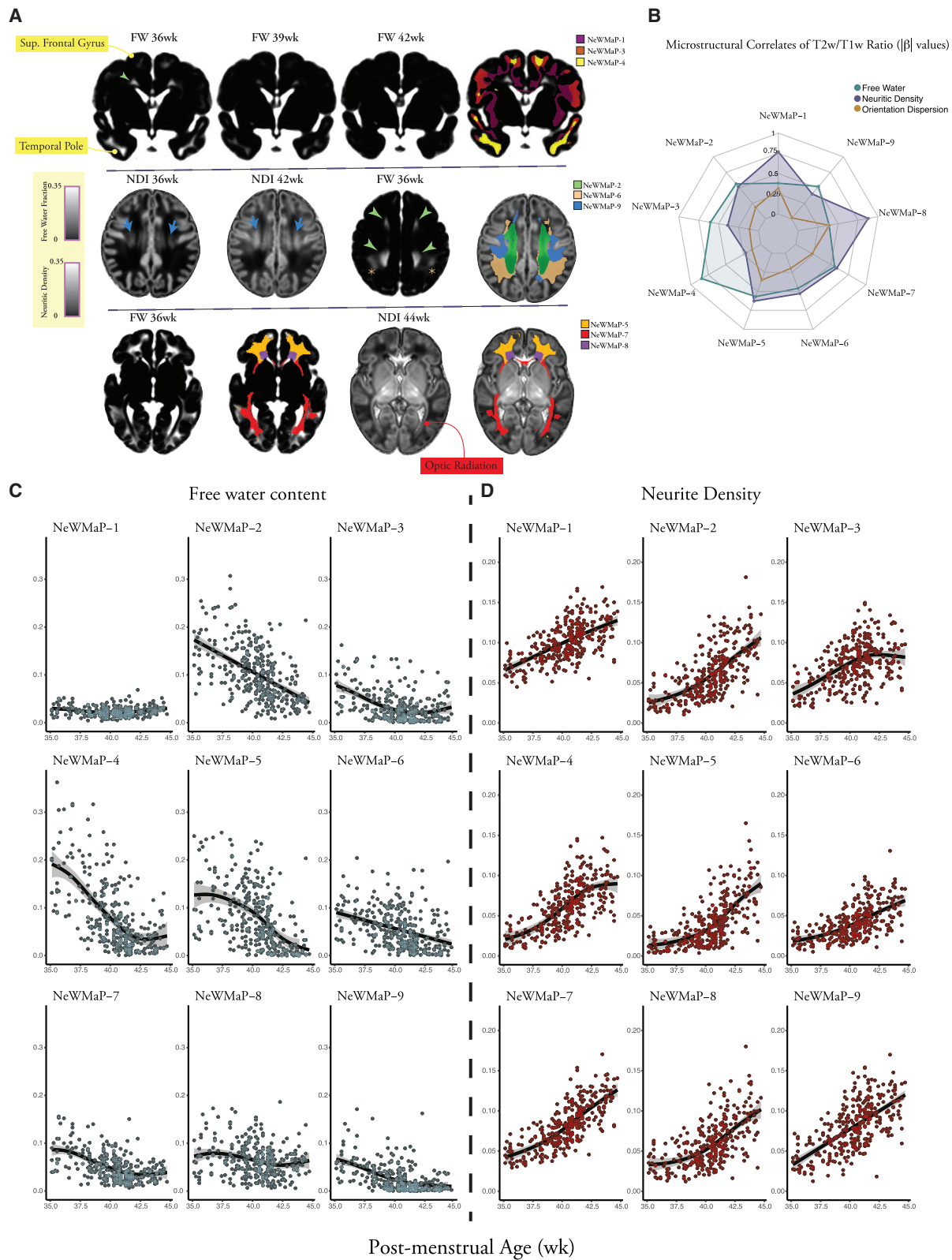
(B) Four dHCP NeWMaPs demonstrated relatively unique correspondence with a single eLAbE factor. NeWMaP-1 also showed a moderate similarity with eLAbE-6 (not shown).

(C) Intermediate/periventricular frontoparietal (NeWMaP-2 and NeWMaP-9) and rostral frontal (NeWMaP-5 and NeWMaP-8) white matter dHCP NeWMaPs merged together and represented by eLAbE-3 and eLAbE-2 factors, respectively.

(D) Superficial white matter NeWMaP-3 split into two eLAbE factors with moderate similarity. Color maps indicate relative loadings for dHCP NeWMaPs and eLAbE factors with warmer colors corresponding to higher values (X-ray colormap is used).

and the dissolution of subplate remnant. These processes can be tracked through qualitative histopathological analysis of post-mortem brain specimens stained for markers of subplate extracellular matrix (Alcian-blue), astrocytes and radial glial cells

(glial fibrillary acidic protein [GFAP]), frontal subventricular zone migrating young neurons (Nissl and doublecortin [DCX]), myelination (myelin basic protein [MBP]), and axonal maturation (phosphorylated neurofilament proteins; SMI 312). Thus, to



(legend on next page)

investigate the neurobiological underpinnings of NeWMaPs, we examined their histological correlates in appropriately stained late fetal/early postnatal brain specimens from the Zagreb Collection of Human Brains ( $n = 8$ ; Table S1) (Hrabač et al., 2018).

Our first goal was to investigate whether variations in NeWMaP  $T_2w/T_1w$  signal and NODDI metrics correlate with the extracellular matrix content in the subplate remnant. The subplate zone is a transient fetal white matter compartment at the interface of the superficial white matter and the cortical ribbon, characterized by abundant and hydrophilic extracellular matrix (Kostović, 2020; Kostović and Judas, 2010), which is selectively stained with Alcian-blue in fetal/postnatal brain (Kostović et al., 2002, 2014). Accordingly, we focused our analysis on the superficial NeWMaPs (NeWMaP 1, 3, and 4) and examined coronal brain sections that included these regions and were stained with Alcian-blue (Figure 5). We observed that Alcian-blue staining in the superficial white matter mirrored the observed higher early postnatal  $T_2w/T_1w$  signal ratio (Figure 2D) and free water content (Figure 3A) in the superficial white matter (NeWMaP-4 > NeWMaP-3 > NeWMaP-1). Specifically, the gyral/superficial white matter (NeWMaP-3 and NeWMaP-4) showed thicker and more intense Alcian-blue staining (particularly in the temporal pole [NeWMaP-4] and gyral crowns) compared with the primarily sulcal superficial white matter (NeWMaP-1) (Figures 5 and S6). Deep white matter structures in NeWMaP-1 (e.g., corpus callosum) showed no or minimal Alcian-blue staining.

Our second goal was to investigate whether differences in periventricular and intermediate white matter cellular elements assessed using GFAP, Nissl, and DCX staining contribute to the delineation of boundaries between adjacent NeWMaPs. Examining brain sections immunostained for GFAP, we observed intense GFAP immunoreactivity in the frontoparietal periventricular region corresponding to NeWMaP-2, which is clearly demarcated from the surrounding white matter by its high early postnatal  $T_2w/T_1w$  signal ratio and free water content (Figures 6A, 6B, and 6C). Adjacent dorsal parietal (NeWMaP-6) and frontoparietal (NeWMaP-9) intermediate white matter compartments, as well as the occipitotemporal periventricular white matter (NeWMaP-7), demonstrated less GFAP immunoreactivity (Figure 6). On the other hand, a distinct feature of the intermediate white matter compartment areas corresponding to NeWMaP-6 and NeWMaP-9 was the presence of radially oriented GFAP-reactive fibers, which likely represent remnants of the radial glial cells (Figure 6D). Rostral frontal periventricular white matter NeWMaP-8 corresponded to the previously

described early postnatal migratory stream within the frontal lobe (Childs et al., 1998; Paredes et al., 2016). The young migrating neurons express DCX and form a cell-dense, cap-like structure along the walls of the frontal horns of the lateral ventricles, referred to as the “arc,” which is also visible on MRI (Paredes et al., 2016) (Figure S2C). In line with these, the white matter corresponding to frontal periventricular NeWMaP-8 was distinguished from the surrounding white matter by Nissl staining and DCX expression (Figures 6E, 6F, and S6).

We also examined MBP and SMI 312 immunostained sections and observed different patterns of myelination and axonal maturation across the NeWMaPs. In the frontoparietal junction, white matter areas corresponding to the NeWMaP-9 and, to a lesser extent, NeWMaP-1 (e.g., corpus callosum and cingulum), showed evidence of myelination (MBP immunoreactivity) and axonal maturation (SMI 312 immunoreactivity), while the NeWMaP-2 frontoparietal periventricular compartment showed no evidence of myelination in early postnatal brains (Figure 7A). Interestingly, while the medial temporal lobe (parahippocampal gyrus and entorhinal cortex) and superficial white matter of the superior temporal gyrus demonstrated intense MBP immunoreactivity, other areas in the temporal lobe showed either modest or no immunoreactivity for MBP. These observations follow the parcellation pattern of the temporal lobe into NeWMaP-1 (medial temporal lobe and superior temporal/Heschl gyrus superficial white matter) and NeWMaP-7 (deep and periventricular white matter), which showed evidence of advanced myelination, as opposed to NeWMaP-3 and NeWMaP-4 (the rest of temporal lobe superficial white matter) (Figure 7B).

## DISCUSSION

In this study, we capitalized on two large developmental cohorts, tailored processing pipelines, advanced multivariate techniques, and flexible modeling to study early postnatal white matter maturation. We showed that the  $T_2w/T_1w$  ratio is a sensitive and robust marker of early postnatal maturation effects. Using unsupervised multivariate pattern analysis, we demonstrated that early postnatal white matter matures in a spatially heterogeneous fashion by integrating highly coordinated units that exhibit differential developmental changes. Importantly, we showed that the derived NeWMaPs are not mere statistical constructs but bear biological significance, and differences in patterning are driven in part by distinct spatiotemporal white matter microstructure changes and correspond to distinct white matter histology (summarized in Table 1).

### Figure 4. Microstructural correlates of the NeWMaPs

(A) Free water, neurite density, and orientation dispersion index (not shown) maps were generated by fitting the NODDI model into the multi-shell diffusion MR images. Weekly average free water and neurite density maps demonstrate patterns of age-related decrease in free water content and increase in neurite density in the early postnatal period. NeWMaPs largely corresponded to distinct tissue microstructure and were well-demarcated on free water and/or neurite density maps. For instance, unlike NeWMaP-1, the other two superficial white matter NeWMaP-3 and NeWMaP-4 showed relatively high free water contents (NeWMaP-4 exhibiting the highest values in the temporal poles and superior frontal gyri). Dorsal frontoparietal periventricular NeWMaP-2 (green arrowheads) was clearly demarcated from the parietal NeWMaP-6 (beige-colored asterisks) and periorlandic NeWMaP-9 (blue arrows) on free water and neurite density maps. The occipital portion of the periventricular NeWMaP-7 corresponded to the high neurite density optic radiations.

(B) Spiderplot showing effects of free water content, neurite density, and orientation dispersion index on  $T_2w/T_1w$  from each NeWMaP.

(C and D) Age-related changes in mean NeWMaP free water content (C) and neurite density (D) in the dHCP cohort. Error bands represent 95% confidence intervals.

# Superficial White Matter NeWMaPs: PAS-Alcian Blue Staining (Extracellular Matrix)

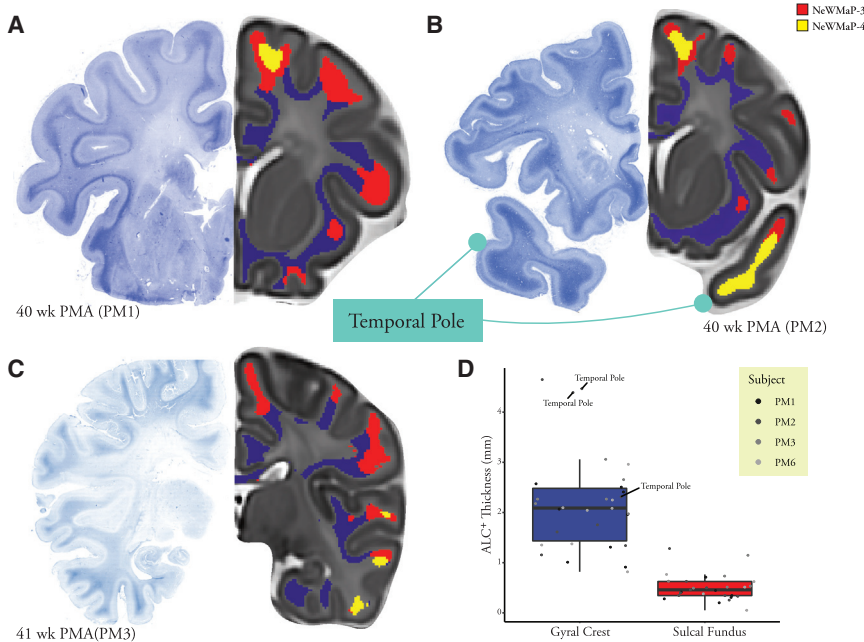


**Figure 5. Extracellular matrix of the subplate remnants with Alcian-blue staining illustrate differences between superficial white matter NeWMaPs**

(A–C) Staining of the extracellular matrix in the subplate remnant with Alcian-blue. Alcian-blue staining of coronal sections through the anterior frontal lobe (A), anterior frontal lobe/temporal pole (B), and frontoparietal junction/posterior temporal lobe (C). Stain vector decomposition was deployed to enhance the Alcian-blue contrast. Corresponding MRI images ( $T_2$ -weighted newborn template) with overlying superficial white matter NeWMaPs (NeWMaP-1, NeWMaP-3, NeWMaP-4) are depicted. Superficial white matter NeWMaP-3 and NeWMaP-4 that localized primarily in the gyri with higher early postnatal  $T_2w/T_1w$  signal ratio and free water content were associated with a more intense and thicker band of Alcian-blue staining (particularly temporal pole [part of NeWMaP-4]). In contrast, sulcal predominant superficial white matter areas corresponding to NeWMaP-1 were associated with thinner and less intense Alcian-blue staining. Deep white matter structures in NeWMaP-1 (e.g., corpus callosum) showed no or minimal Alcian-blue staining.

(D) Boxplots showing significantly thicker Alcian-blue positive bands underneath the cortical ribbon

at the gyral crests compared with the sulcal fundi (particularly in the temporal pole;  $p < 0.001$ ). Boxplot center lines represent median; the lower and upper hinges correspond to the 25th and 75th percentiles; the lower/upper whisker extends from the hinge to the smallest/largest value no further than 1.5 × inter-quartile range.

See also Figure S6.

We confirmed that by simply dividing  $T_2w$  images by  $T_1w$  images, it is possible to generate quantitative maps of white matter maturation during the early postnatal period. Additionally, we showed that these maps are sensitive to the early postnatal maturation effects, robust across different MR imaging settings (similar results across two independent large cohorts with different MR imaging platforms, sequences, and resolutions), and reflect spatial variations in white matter microstructure and histological markers of white matter maturation. Our findings demonstrate that various microstructural (i.e., neurite density and free water content) and histological (i.e., myelination, extracellular matrix, and glial cell pattern and density) factors contribute to the observed  $T_2w/T_1w$  signal ratio variations in the early postnatal period. Therefore, early postnatal white matter  $T_2w/T_1w$  signal ratio variations should be interpreted in their spatial contexts, as these variations tend to represent distinct underlying histology in different white matter compartments (e.g., periventricular versus superficial white matter).

Accordingly, we investigated the spatial variations of  $T_2w/T_1w$  signal ratio in the dHCP dataset using NMF. We were able to identify reproducible and coherent patterns of white matter signal evolution in the neonatal brain at multiple scales using a data-driven approach. Moreover, similar early postnatal white matter maturation patterns ( $K = 9$ ) also re-emerged from the eLABE dataset despite differences in image acquisition techniques and demographic characteristics of the dHCP and eLABE datasets. The merging of four dHCP NeWMaPs into two distinct white matter maturational patterns derived from eLABE may have stemmed from lower image acquisition resolution in the

eLABE study (0.8 mm isotropic voxels versus 0.5 mm isotropic voxels in dHCP) that can, in turn, hamper the distinction of adjacent periventricular and intermediate NeWMaPs.

Our approach does not implement any hierarchical constraints, is blind to location in space, and is not biased by a preconceived model of white matter development or white matter tracts. However, estimated NeWMaPs at higher resolutions demonstrated increasing differentiation, while largely respecting the boundaries of coarser subdivisions and being predominantly symmetric bilaterally. Importantly, NeWMaPs exhibited a distinctive range of distances from the lateral ventricles and/or the cortex and were not confined to distinct white matter tracts. Of note, this was not a mere byproduct of our registration approach, as we observed similar patterns without considering distances to the cortex and lateral ventricles for registration. In addition, the majority of the NeWMaPs were not limited to a specific brain lobe or overlying cortical structure. Instead, NeWMaPs were aligned with white matter compartments (Kostović et al., 2014), analogous to the laminar and segmental reorganization of the fetal white matter (von Monakow, 1905; Žunić Išasegi et al., 2018).

Each NeWMaP demonstrated a characteristic  $T_2w/T_1w$  signal ratio evolution pattern in early postnatal development. Although other studies have indicated that sex effects on brain volumetric growth may occur as early as early in the fetal period (Studholme et al., 2020), our results suggest that sex effects (main effects or sex-by-age interaction effects) likely have minor impact (if any) on the evolution of cerebral white matter  $T_2w/T_1w$  signal ratio during the early postnatal period. Intriguingly, prematurity had the strongest effects on NeWMaP-1, NeWMaP-3, and

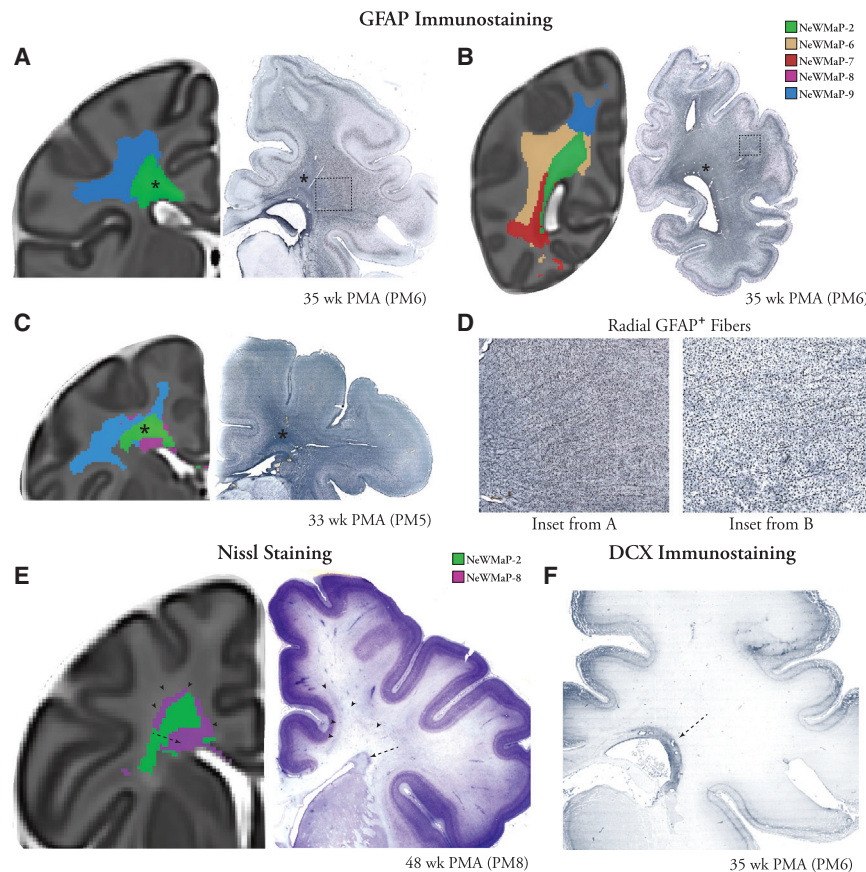


**Figure 6. Distinct cellular elements in the periventricular and intermediate NeWMaPs** (A–D) Glial fibrillary acidic protein (GFAP) immunohistochemistry of the glial cells. Coronal sections through the frontoparietal junction (A), mid-parietal lobe (B), and posterior frontal lobe (C). (A–C) The dorsal frontoparietal periventricular NeWMaP-2 is demarcated from the surrounding parietal and periroladic intermediate white matter NeWMaPs (NeWMaP-6 and NeWMaP-9) and rostral frontal periventricular NeWMaP-8 by its intense GFAP immunoreactivity (marked by asterisk). (D) A distinct feature of the intermediate white matter compartment areas corresponding to NeWMaP-6 and NeWMaP-9 was the presence of radially oriented GFAP-reactive fibers, which likely represent remnants of the radial glial cells. (E) NeWMaP-8 is distinguished from the surrounding frontal white matter (e.g., NeWMaP-2) by Nissl staining (dashed arrow). A fine band of faint Nissl staining in the deep white matter was also represented by NeWMaP-8 (arrowheads). (F) Stain vector decomposition demonstrated doublecortin (DCX, a marker of young migrating neurons) expression in frontal periventricular white matter NeWMaP-8 (dashed arrow). See also Figure S6.

NeWMaP-9 that also showed the slowest rate of decline in  $T_2w/T_1w$  signal ratio after 38 weeks postmenstrual age, suggesting that these NeWMaPs are at a more developed stage at term and that the late fetal period is more crucial for their maturation. These findings were consistent with earlier reports showing association of preterm birth with increased diffusivity or  $T_2$  prolongation in earlier-myelinating white matter tracts such as the corpus callosum, cingulum bundle, and external capsule (part of NeWMaP-1), and corticospinal tract and superior longitudinal fasciculus (part of NeWMaP-9) (Eikenes et al., 2011; Knight et al., 2018).

Importantly, we demonstrated that the derived NeWMaPs reflect distinct underlying microstructural and histological features. We found that low  $T_2w/T_1w$  signal ratios and high neurite density in white matter structures corresponded to areas of early postnatal myelination (Brody et al., 1987) (e.g., superior temporal gyrus and auditory radiation [NeWMaP-1] and optic radiations [NeWMaP-7]). However, human white matter myelination is a slow and protracted process with its most rapid and dramatic period occurring within the first two years of postnatal life (Kinney and Volpe, 2018; Miller et al., 2012). Therefore, our findings from the early postnatal period capture only a small segment of the extended myelination process. Taken together, these may explain why early postnatal patterns of white matter signal evolution transcended white matter tract definitions and were aligned instead with white matter compartments.

NeWMaP-3 and NeWMaP-4 correspond to the subplate remnant. Previous postmortem histology and fetal/postnatal MRI studies have shown that the dissolution of the subplate starts from the sulcal areas, resulting in a thinner, “band-like” appearance in sulci and thicker, diffuse appearance in gyral white matter in the early postnatal period (Kostović et al., 2014). We observed a similar distinction between primarily sulcal superficial white matter (NeWMaP-1) and gyral superficial white matter (NeWMaP-3 and NeWMaP-4), with the latter exhibiting higher free water content and  $T_2w/T_1w$  signal ratio. This is in line with previous studies that have shown that the subplate compartment appears hyperintense on  $T_2w$  images and is characterized by high free water content, as estimated from diffusion-weighted MRI, due to its abundant hydrophilic extracellular matrix composition (Kostović, 2020; Kostović et al., 2014). Abundance of extracellular matrix in the subplate remnant compartment is a marker of growth of short corticocortical pathways, especially U-shape fibers, which are known to develop postnatally (Burkhalter et al., 1993; Huang et al., 2009; Vasung et al., 2017).

The correlation of MR imaging and histologic findings also provided insight into the organization of the periventricular crossroad areas (Judas et al., 2005; Pittet et al., 2019). We observed a radial demarcation of the frontoparietal white matter into the periventricular NeWMaP-2 (corresponding to the dorsal frontoparietal crossroad area) from the surrounding intermediate white matter.

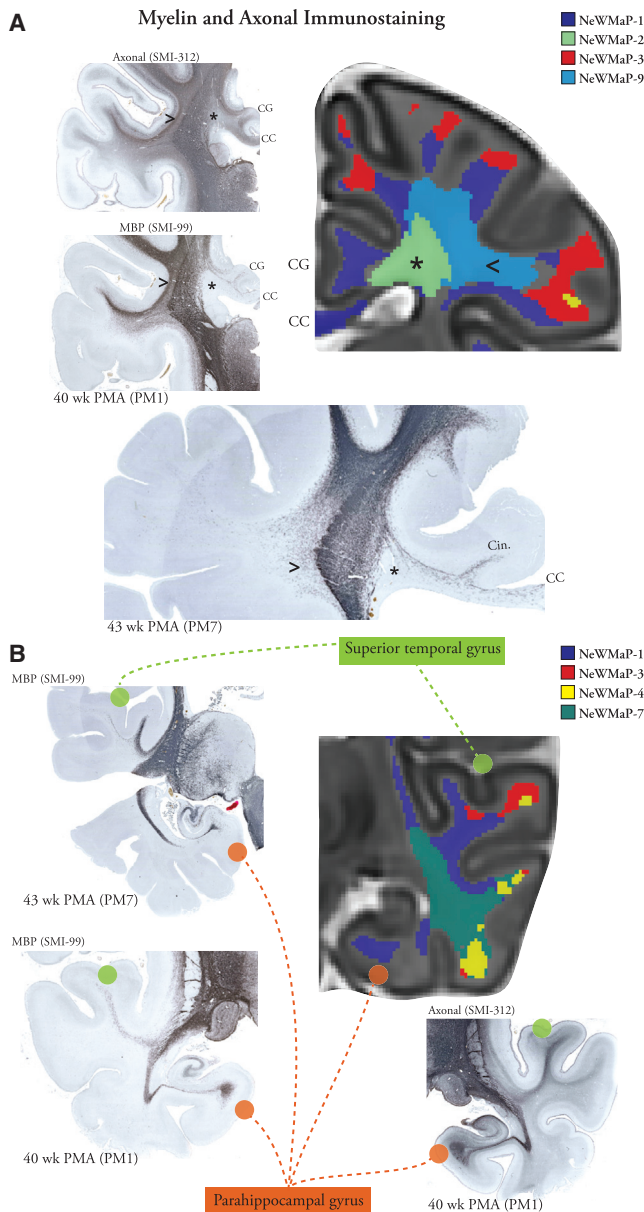


**Figure 7. Different patterns of myelination and axonal maturation across the NeWMaPs**

(A) Unlike intermediate white matter compartment NeWMaP-9 (marked by <), periventricular NeWMaP-2 (marked by asterisk) showed no evidence of advanced myelination (no myelin basic protein [MBP] immunoreactivity) and less axonal maturation (less SMI 312 immunoreactivity). Corpus callosum (CC) and white matter associated with the cingulate gyrus (CG; both parts of NeWMaP-1) exhibited axonal maturation and myelination.

(B) Medial temporal lobe (parahippocampal gyrus and entorhinal cortex) and superior temporal gyrus superficial white matter areas corresponding to the NeWMaP-1 showed MBP immunoreactivity, whereas other temporal superficial white matter areas showed no or minimal immunoreactivity. Deep temporal lobe white matter areas showing MBP immunoreactivity either corresponded to NeWMaP-7 or NeWMaP-1. See also Figure S6.

Specifically, the periventricular NeWMaP-2 was characterized by high  $T_2w/T_1w$  signal ratio, free water content, and GFAP staining. In contrast, NeWMaP-6 and NeWMaP-9 were less GFAP intense, showed more advanced myelination, and were characterized by the presence of radially oriented GFAP-reactive fibers that likely represent remnants of radial glial cells. Together, these findings suggest that distinct patterns and extents of glial cell GFAP reactivity can be associated with noticeable differences in  $T_2w/T_1w$  signal ratio. These differences likely arise from the role of radial glial cells and astrocytes in the production and maintenance of the extracellular matrix during brain development (Wiese et al., 2012). Periventricular astrocytes and radial glial cells play key roles in fetal brain development, such as neurogenesis and neural migration (Hansen et al., 2010; Nadarajah and Parnavelas, 2002). Finally, we showed that the signal evolution pattern in the frontal periventricular white matter (NeWMaP-8) likely corresponds to the frontal lobe neural migration that continues for several months after birth (Paredes et al., 2016; Sanai et al., 2011). However, the significance of the radial glial cells observed in the intermediate parietal white matter remains unclear. Therefore, additional studies are needed to investigate whether postnatal neural migration also occurs in the parietal lobes, potentially contributing to these observed signal variations.

Although this study capitalized on a large sample and advanced methods, certain limitations should be noted. First, the  $T_2w/T_1w$  signal intensity ratio is an indirect measure of tissue relaxation times. Relaxometry methods (Leppert et al., 2009) could provide a clearer interpretation of the signal changes. However, these are not widely used in clinical settings, whereas advances in fast and high-resolution acquisition of T1w and T2w MR sequences have improved the feasibility of imaging neonatal patients (Kozak et al., 2020). Second, while we included preterm-born newborns in our study, we performed our analyses in MR images from healthy newborns without incidental neuroimaging findings of clinical significance. It remains to be determined whether this approach can also be applied to a wider clinical setting to identify abnormal patterns of postnatal white matter signal evolution in various conditions. Lastly, while we primarily focused on the 9-pattern solution as the simplest solution with high split-half reliability, the optimal number of patterns to describe early postnatal  $T_2w/T_1w$  signal intensity ratio evolution is likely a function of MR imaging acquisition technique (e.g., image resolution, signal/contrast-to-noise ratio,  $T_2w$  and  $T_1w$  weighting), age range, and demographics of the newborns. Moreover, different resolutions may be most useful for certain clinical and/or research applications (e.g., brain injury, developmental abnormalities). Therefore, we have provided all NMF results at 2–20 resolutions as a resource for the newborn neuroimaging community (deposited at Zenodo: <https://doi.org/10.5281/zenodo.6782004>).

These limitations notwithstanding, the identified early postnatal maturational patterns may provide an alternative to existing tract-based atlas definitions for this critical neurodevelopmental period. By providing a concise representation of early postnatal white matter maturation, these patterns can be exploited to examine the influence of the complex high dimensional genetic and environmental factors on brain development. We further provide normative age trajectories of signal ratio in these NeWMaPs, which can be used to monitor white matter signal

**Table 1. Distinctive  $T_2w/T_1w$  signal, early postnatal microstructural, and histological characteristics of the NeWMaPs**

	NeWMaPs	Anatomical	$T_2w/T_1w$ : decline rate/early postnatal value	Early postnatal FW/NDI	Histological features <sup>a</sup>
Superficial	NeWMaP-1	sulcal, callosal, and limbic	slow/very low	very low/high	ALB <sup>-</sup> /MBP <sup>++</sup>
	NeWMaP-3	gyral-nonlocalized	slow/low	intermediate/intermediate	ALB <sup>+</sup> /MBP <sup>-</sup>
	NeWMaP-4	gyral-temporal pole and SFG	fast/high	high/intermediate	ALB <sup>++</sup> /MBP <sup>-</sup>
Periventricular	NeWMaP-2	dorsal frontoparietal	fast/high	high/intermediate	GFAP <sup>++</sup> /MBP <sup>-</sup>
	NeWMaP-7	occipitotemporal-optic radiation	intermediate/ intermediate	intermediate/high	GFAP <sup>+</sup> /MBP <sup>+</sup>
	NeWMaP-8	rostral frontal	intermediate/high	intermediate/intermediate	Nissl <sup>+</sup> /DCX <sup>+</sup> /GFAP <sup>-</sup>
Intermediate	NeWMaP-5	frontal	fast/high	intermediate/low	MBP <sup>-</sup>
	NeWMaP-6	parietal	intermediate/high	intermediate/low	radial GFAP <sup>+</sup> fibers
	NeWMaP-9	perirolandic	intermediate/low	intermediate/high	radial GFAP <sup>+</sup> fibers/MBP <sup>+</sup>

ALB, Alcian-Blue; DCX, Doublecortin; GFAP, glial fibrillary acidic protein; MBP, myelin basic protein immunohistochemistry; SFG, superior frontal gyrus.

<sup>a</sup>The distinctive histological features are based on the available histological slides (no MBP slides were available for NeWMaP-6 and NeWMaP-8; no GFAP slide was available for NeWMaP-5).

evolution during early postnatal development. Additionally, our findings suggest that the maturational patterns are rooted in histological variations across the white matter, largely recapitulating late fetal/early postnatal white matter organization. Taken together, the derived spatial patterns and corresponding developmental trajectories provide important context that can inform neurobiological studies of early postnatal development in health and disease and guide clinical studies of early life therapeutic interventions (Baak et al., 2022). In conclusion, our study provides insights into early postnatal white matter organization and maturation using high-resolution  $T_2w$  and  $T_1w$  MRI sequences coupled with advanced image processing and analysis techniques. We reveal distinct white matter maturation patterns, which follow distinct developmental trajectories and align well with the underlying microstructure and histology.

## STAR★METHODS

Detailed methods are provided in the online version of this paper and include the following:

- **KEY RESOURCES TABLE**
- **RESOURCE AVAILABILITY**
  - Lead contact
  - Materials availability
  - Data and code availability
- **EXPERIMENTAL MODEL AND SUBJECT DETAILS**
  - The developing human connectome project
  - The early life adversity, biological embedding, and risk for developmental precursors of mental disorders (eLAbE) study
  - The zagreb collection of human brains
- **METHOD DETAILS**
  - $T_1w$  and  $T_2w$  MRI acquisition
  - $T_2w/T_1w$  map generation, preprocessing, and registration

- Diffusion-weighted MRI and NODDI
- MRI acquisition and image analysis in the eLAbE study
- Histological analysis
- **QUANTIFICATION AND STATISTICAL ANALYSIS**
  - Non-negative matrix factorization
  - Statistical analysis

## SUPPLEMENTAL INFORMATION

Supplemental information can be found online at <https://doi.org/10.1016/j.neuron.2022.09.020>.

## ACKNOWLEDGMENTS

A.N. was supported by Canon Medical Systems USA, Inc./Radiological Society of North America Research & Education (RSNA R&E) Foundation Research Resident Grant (RR1953) and Foundation of the American Society of Neuroradiology (ASNR) Grant Program. A.S. was partially supported by the National Institutes of Health (NIH) award R01AG067103. J.S.S. was supported by NIH award P50 HD103525 to the Intellectual and Developmental Disabilities Research Center at Washington University. Data were provided by the developing Human Connectome Project, KCL-Imperial-Oxford Consortium funded by the European Research Council under the European Union Seventh Framework Programme (FP/2007-2013)/ERC grant agreement no. 319456. We are grateful to the families who generously supported this trial. The eLAbE study was supported by NIH award R01MH113883. This research was partly funded by the Research Cooperability Program of the Croatian Science Foundation funded by the European Union from the European Social Fund under the Operational Programme Efficient Human Resources 2014-2020 PSZ-2019-02-4710 (Z.K.). Computations were performed using the facilities of the Washington University Center for High Performance Computing, which were partially funded by NIH grants 1S10RR022984-01A1 and 1S10OD018091-01.

## AUTHOR CONTRIBUTIONS

Conceptualization, A.N. and A.S.; methodology, A.N., Z.K., I.K., S.M.H., D.M.B., C.D.S., and A.S.; investigation, A.N., Z.K., I.K., J.K., D.A., C.D.S., and A.S.; data curation, A.N., Z.K., D.A., S.K., and D.M.; formal analysis, A.N. and A.S.; writing—original draft, A.N. and A.S.; writing—review & editing, A.N., Z.K., I.K., S.M.H., J.K., D.A., S.K., D.M., J.L.L., B.B.W., C.E.R., D.M.B.,

J.S.S., R.C.M., J.J.N., C.D.S., and A.S.; visualization, A.N. and Z.K.; resources, Z.K., C.D.S., and A.S.

## DECLARATION OF INTERESTS

A.S. holds equity in TheraPanacea and has received personal compensation for serving on the Alzheimer's Disease Research Program Scientific Review Committee of the BrightFocus Foundation.

## INCLUSION AND DIVERSITY

We support inclusive, diverse, and equitable conduct of research.

Received: April 19, 2022

Revised: August 19, 2022

Accepted: September 15, 2022

Published: October 14, 2022

## REFERENCES

- Adamson, C.L., Alexander, B., Ball, G., Beare, R., Cheong, J.L.Y., Spittle, A.J., Doyle, L.W., Anderson, P.J., Seal, M.L., and Thompson, D.K. (2020). Parcellation of the neonatal cortex using Surface-based Melbourne Children's Regional Infant Brain atlases (M-CRIB-S). *Sci. Rep.* **10**, 4359. <https://doi.org/10.1038/s41598-020-61326-2>.
- Alexander, B., Kelly, C.E., Adamson, C., Beare, R., Zannino, D., Chen, J., Murray, A.L., Loh, W.Y., Matthews, L.G., Warfield, S.K., et al. (2019). Changes in neonatal regional brain volume associated with preterm birth and perinatal factors. *Neuroimage* **185**, 654–663. <https://doi.org/10.1016/j.neuroimage.2018.07.021>.
- Andersson, J.L.R., and Sotiropoulos, S.N. (2016). An integrated approach to correction for off-resonance effects and subject movement in diffusion MR imaging. *Neuroimage* **125**, 1063–1078. <https://doi.org/10.1016/j.neuroimage.2015.10.019>.
- Avants, B.B., Tustison, N.J., Song, G., Cook, P.A., Klein, A., and Gee, J.C. (2011). A reproducible evaluation of ANTs similarity metric performance in brain image registration. *Neuroimage* **54**, 2033–2044. <https://doi.org/10.1016/j.neuroimage.2010.09.025>.
- Baak, L.M., Wagenaar, N., van der Aa, N.E., Groenendaal, F., Dudink, J., Tataranno, M.L., Mahamud, U., Verhage, C.H., Eijssers, R.M.J.C., Smit, L.S., et al. (2022). Feasibility and safety of intranasally administered mesenchymal stromal cells after perinatal arterial ischaemic stroke in the Netherlands (PASSION): a first-in-human, open-label intervention study. *Lancet Neurol.* **21**, 528–536. [https://doi.org/10.1016/S1474-4422\(22\)00117-X](https://doi.org/10.1016/S1474-4422(22)00117-X).
- Bankhead, P., Loughrey, M.B., Fernández, J.A., Dombrowski, Y., McArt, D.G., Dunne, P.D., McQuaid, S., Gray, R.T., Murray, L.J., Coleman, H.G., et al. (2017). QuPath: open source software for digital pathology image analysis. *Sci. Rep.* **7**, 16878. <https://doi.org/10.1038/s41598-017-17204-5>.
- Barkovich, M.J., and Barkovich, A.J. (2019). MR imaging of normal brain development. *Neuroimaging Clin. N. Am.* **29**, 325–337. <https://doi.org/10.1016/j.nic.2019.03.007>.
- Bastiani, M., Andersson, J.L.R., Cordero-Grande, L., Murgasova, M., Hutter, J., Price, A.N., Makropoulos, A., Fitzgibbon, S.P., Hughes, E., Rueckert, D., et al. (2019). Automated processing pipeline for neonatal diffusion MRI in the developing Human Connectome Project. *Neuroimage* **185**, 750–763. <https://doi.org/10.1016/j.neuroimage.2018.05.064>.
- Brenner, R.G., Smyser, C.D., Lean, R.E., Kenley, J.K., Smyser, T.A., Cyr, P.E.P., Shimony, J.S., Barch, D.M., and Rogers, C.E. (2021). Microstructure of the dorsal anterior cingulum bundle in very preterm neonates predicts the preterm behavioral phenotype at 5 years of age. *Biol. Psychiatry* **89**, 433–442. <https://doi.org/10.1016/j.biopsych.2020.06.015>.
- Brody, B.A., Kinney, H.C., Kloman, A.S., and Gilles, F.H. (1987). Sequence of central nervous system myelination in human infancy. I. An autopsy study of myelination. *J. Neuropathol. Exp. Neurol.* **46**, 283–301. <https://doi.org/10.1097/00005072-198705000-00005>.
- Brunet, J.P., Tamayo, P., Golub, T.R., and Mesirov, J.P. (2004). Metagenes and molecular pattern discovery using matrix factorization. *Proc. Natl. Acad. Sci. USA* **101**, 4164–4169. <https://doi.org/10.1073/pnas.0308531101>.
- Burkhalter, A., Bernardo, K.L., and Charles, V. (1993). Development of local circuits in human visual cortex. *J. Neurosci.* **13**, 1916–1931. <https://doi.org/10.1523/JNEUROSCI.13-05-01916.1993>.
- Childs, A.M., Ramenghi, L.A., Evans, D.J., Ridgeway, J., Saysell, M., Martinez, D., Arthur, R., Tanner, S., and Levene, M.I. (1998). MR features of developing periventricular white matter in preterm infants: evidence of glial cell migration. *AJNR Am. J. Neuroradiol.* **19**, 971–976.
- Corbett-Detig, J., Habas, P.A., Scott, J.A., Kim, K., Rajagopalan, V., McQuillen, P.S., Barkovich, A.J., Glenn, O.A., and Studholme, C. (2011). 3D global and regional patterns of human fetal subplate growth determined in utero. *Brain Struct. Funct.* **215**, 255–263. <https://doi.org/10.1007/s00429-010-0286-5>.
- Cordero-Grande, L., Hughes, E.J., Hutter, J., Price, A.N., and Hajnal, J.V. (2018). Three-dimensional motion corrected sensitivity encoding reconstruction for multi-shot multi-slice MRI: application to neonatal brain imaging. *Magn. Reson. Med.* **79**, 1365–1376.
- Cox, R.W. (2012). AFNI: what a long strange trip it's been. *Neuroimage* **62**, 743–747. <https://doi.org/10.1016/j.neuroimage.2011.08.056>.
- Dean, D.C., 3rd, Planalp, E.M., Wooten, W., Adluru, N., Kecskemeti, S.R., Frye, C., Schmidt, C.K., Schmidt, N.L., Styner, M.A., Goldsmith, H.H., et al. (2017). Mapping white matter microstructure in the one month human brain. *Sci. Rep.* **7**, 9759. <https://doi.org/10.1038/s41598-017-09915-6>.
- Dubois, J., Dehaene-Lambertz, G., Kulikova, S., Poupon, C., Hüppi, P.S., and Hertz-Pannier, L. (2014). The early development of brain white matter: a review of imaging studies in fetuses, newborns and infants. *Neuroscience* **276**, 48–71. <https://doi.org/10.1016/j.neuroscience.2013.12.044>.
- Eickhoff, S.B., Yeo, B.T.T., and Genov, S. (2018). Imaging-based parcellations of the human brain. *Nat. Rev. Neurosci.* **19**, 672–686. <https://doi.org/10.1038/s41583-018-0071-7>.
- Eikenes, L., Lohaugen, G.C., Brubakk, A.M., Skranes, J., and Håberg, A.K. (2011). Young adults born preterm with very low birth weight demonstrate widespread white matter alterations on brain DTI. *Neuroimage* **54**, 1774–1785. <https://doi.org/10.1016/j.neuroimage.2010.10.037>.
- Fleiss, J.L., Levin, B., and Paik, M.C. (2013). *Statistical methods for rates and proportions* (John Wiley & Sons).
- Gilmore, J.H., Knickmeyer, R.C., and Gao, W. (2018). Imaging structural and functional brain development in early childhood. *Nat. Rev. Neurosci.* **19**, 123–137. <https://doi.org/10.1038/nrn.2018.1>.
- Gilmore, J.H., Lin, W., Corouge, I., Vetsa, Y.S.K., Smith, J.K., Kang, C., Gu, H., Hamer, R.M., Lieberman, J.A., and Gerig, G. (2007). Early postnatal development of corpus callosum and corticospinal white matter assessed with quantitative tractography. *AJNR Am. J. Neuroradiol.* **28**, 1789–1795. <https://doi.org/10.3174/ajnr.a0751>.
- Glasser, M.F., Sotiropoulos, S.N., Wilson, J.A., Coalson, T.S., Fischl, B., Andersson, J.L., Xu, J., Jbabdi, S., Webster, M., Polimeni, J.R., et al. (2013). The minimal preprocessing pipelines for the Human Connectome Project. *Neuroimage* **80**, 105–124.
- Glasser, M.F., and Van Essen, D.C. (2011). Mapping human cortical areas in vivo based on myelin content as revealed by T1- and T2-weighted MRI. *J. Neurosci.* **31**, 11597–11616. <https://doi.org/10.1523/JNEUROSCI.2180-11.2011>.
- Guma, E., Plitman, E., and Chakravarty, M.M. (2019). The role of maternal immune activation in altering the neurodevelopmental trajectories of offspring: A translational review of neuroimaging studies with implications for autism spectrum disorder and schizophrenia. *Neurosci. Biobehav. Rev.* **104**, 141–157. <https://doi.org/10.1016/j.neubiorev.2019.06.020>.
- Hansen, D.V., Lui, J.H., Parker, P.R.L., and Kriegstein, A.R. (2010). Neurogenic radial glia in the outer subventricular zone of human neocortex. *Nature* **464**, 554–561. <https://doi.org/10.1038/nature08845>.

- Harms, R.L., Fritz, F.J., Tobisch, A., Goebel, R., and Roebroeck, A. (2017). Robust and fast nonlinear optimization of diffusion MRI microstructure models. *Neuroimage* 155, 82–96. <https://doi.org/10.1016/j.neuroimage.2017.04.064>.
- Harms, R.L., and Roebroeck, A. (2018). Robust and fast Markov chain Monte Carlo sampling of diffusion MRI microstructure models. *Front. Neuroinform.* 12, 97. <https://doi.org/10.3389/fninf.2018.00097>.
- Hazlett, H.C., Gu, H., Munsell, B.C., Kim, S.H., Styner, M., Wolff, J.J., Elison, J.T., Swanson, M.R., Zhu, H., Botteron, K.N., et al. (2017). Early brain development in infants at high risk for autism spectrum disorder. *Nature* 542, 348–351. <https://doi.org/10.1038/nature21369>.
- Hrabac, P., Bosak, A., Vuksić, M., Judaš, M., Kostović, I., and Kršnik, Ž. (2018). The Zagreb Collection of human brains: entering the virtual world. *Croat. Med. J.* 59, 283–287. <https://doi.org/10.3325/cmj.2018.59.283>.
- Huang, H., Xue, R., Zhang, J., Ren, T., Richards, L.J., Yarowsky, P., Miller, M.I., and Mori, S. (2009). Anatomical characterization of human fetal brain development with diffusion tensor magnetic resonance imaging. *J. Neurosci.* 29, 4263–4273. <https://doi.org/10.1523/JNEUROSCI.2769-08.2009>.
- Huang, X., Paragios, N., and Metaxas, D.N. (2006). Shape registration in implicit spaces using information theory and free form deformations. *IEEE Trans. Pattern Anal. Mach. Intell.* 28, 1303–1318. <https://doi.org/10.1109/TPAMI.2006.171>.
- Hubert, L., and Arabie, P. (1985). Comparing partitions. *J. Classif.* 2, 193–218. <https://doi.org/10.1007/BF01908075>.
- Hughes, E.J., Winchman, T., Padormo, F., Teixeira, R., Wurie, J., Sharma, M., Fox, M., Hutter, J., Cordero-Grande, L., Price, A.N., et al. (2017). A dedicated neonatal brain imaging system. *Magn. Reson. Med.* 78, 794–804. <https://doi.org/10.1002/mrm.26462>.
- Jenkinson, M., Beckmann, C.F., Behrens, T.E.J., Woolrich, M.W., and Smith, S.M. (2012). FSL. *Neuroimage* 62, 782–790. <https://doi.org/10.1016/j.neuroimage.2011.09.015>.
- Judas, M., Rados, M., Jovanov-Milosevic, N., Hrabac, P., Stern-Padovan, R., and Kostovic, I. (2005). Structural, immunocytochemical, and mr imaging properties of periventricular crossroads of growing cortical pathways in preterm infants. *AJNR Am. J. Neuroradiol.* 26, 2671–2684.
- Kinney, H.C., and Volpe, J.J. (2018). Chapter 8. Myelination events. In *Volpe's neurology of the newborn, Sixth Edition*, J.J. Volpe, T.E. Inder, B.T. Darras, L.S. de Vries, A.J. du Plessis, J.J. Neil, and J.M. Perlman, eds. (Elsevier), pp. 176–188.
- Knight, M.J., Smith-Collins, A., Newell, S., Denbow, M., and Kauppinen, R.A. (2018). Cerebral white matter maturation patterns in preterm infants: an MRI T2 relaxation anisotropy and diffusion tensor imaging study. *J. Neuroimaging* 28, 86–94. <https://doi.org/10.1111/jon.12486>.
- Kostović, I. (2020). The enigmatic fetal subplate compartment forms an early tangential cortical nexus and provides the framework for construction of cortical connectivity. *Prog. Neurobiol.* 194, 101883. <https://doi.org/10.1016/j.pneurobio.2020.101883>.
- Kostović, I., Jovanov-Milošević, N., Radoš, M., Sedmak, G., Benjak, V., Kostović-Srzić, M., Vasung, L., Čuljat, M., Radoš, M., Hüppi, P., and Judaš, M. (2014). Perinatal and early postnatal reorganization of the subplate and related cellular compartments in the human cerebral wall as revealed by histological and MRI approaches. *Brain Struct. Funct.* 219, 231–253. <https://doi.org/10.1007/s00429-012-0496-0>.
- Kostović, I., and Judas, M. (2010). The development of the subplate and thalamocortical connections in the human foetal brain. *Acta Paediatr.* 99, 1119–1127. <https://doi.org/10.1111/j.1651-2227.2010.01811.x>.
- Kostović, I., Judas, M., Rados, M., and Hrabac, P. (2002). Laminar organization of the human fetal cerebrum revealed by histochemical markers and magnetic resonance imaging. *Cereb. Cortex* 12, 536–544. <https://doi.org/10.1093/cercor/12.5.536>.
- Kostović, I., Kostović-Srzić, M., Benjak, V., Jovanov-Milošević, N., and Radoš, M. (2014). Developmental dynamics of radial vulnerability in the cerebral compartments in preterm infants and neonates. *Front. Neurol.* 5, 139. <https://doi.org/10.3389/fneur.2014.00139>.
- Kozak, B.M., Jaimes, C., Kirsch, J., and Gee, M.S. (2020). MRI techniques to decrease imaging times in children. *RadioGraphics* 40, 485–502. <https://doi.org/10.1148/rj.2020190112>.
- Kuklisova-Murgasova, M., Quaghebeur, G., Rutherford, M.A., Hajnal, J.V., and Schnabel, J.A. (2012). Reconstruction of fetal brain MRI with intensity matching and complete outlier removal. *Med. Image Anal.* 16, 1550–1564. <https://doi.org/10.1016/j.media.2012.07.004>.
- Kunz, N., Zhang, H., Vasung, L., O'Brien, K.R., Assaf, Y., Lazeyras, F., Alexander, D.C., and Hüppi, P.S. (2014). Assessing white matter microstructure of the newborn with multi-shell diffusion MRI and biophysical compartment models. *Neuroimage* 96, 288–299. <https://doi.org/10.1016/j.neuroimage.2014.03.057>.
- Lange, T., Roth, V., Braun, M.L., and Buhmann, J.M. (2004). Stability-based validation of clustering solutions. *Neural Comput.* 16, 1299–1323. <https://doi.org/10.1162/089976604773717621>.
- Lee, D.D., and Seung, H.S. (1999). Learning the parts of objects by non-negative matrix factorization. *Nature* 401, 788–791. <https://doi.org/10.1038/44565>.
- Lee, K., Cherel, M., Budin, F., Gilmore, J., Consing, K.Z., Rasmussen, J., Wadhwa, P.D., Entringer, S., Glasser, M.F., Van Essen, D.C., et al. (2015). Early postnatal myelin content estimate of white matter via T1w/T2w ratio. *Proc. SPIE Int. Soc. Opt. Eng.* 9417, 94171R. <https://doi.org/10.1117/12.2082198>.
- Leppert, I.R., Almli, C.R., McKinstry, R.C., Mulkern, R.V., Pierpaoli, C., Rivkin, M.J., and Pike, G.B.; Brain Development Cooperative Group (2009). T(2) relaxation of normal pediatric brain development. *J. Magn. Reson. Imaging* 29, 258–267. <https://doi.org/10.1002/jmri.21646>.
- Makropoulos, A., Aljabar, P., Wright, R., Hüning, B., Merchant, N., Arichi, T., Tsur, N., Hajnal, J.V., Edwards, A.D., Counsell, S.J., and Rueckert, D. (2016). Regional growth and atlas of the developing human brain. *Neuroimage* 125, 456–478. <https://doi.org/10.1016/j.neuroimage.2015.10.047>.
- Makropoulos, A., Gousias, I.S., Ledig, C., Aljabar, P., Serag, A., Hajnal, J.V., Edwards, A.D., Counsell, S.J., and Rueckert, D. (2014). Automatic whole brain MRI segmentation of the developing neonatal brain. *IEEE Trans. Med. Imaging* 33, 1818–1831. <https://doi.org/10.1109/TMI.2014.2322280>.
- Makropoulos, A., Robinson, E.C., Schuh, A., Wright, R., Fitzgibbon, S., Bozek, J., Counsell, S.J., Steinweg, J., Vecchiato, K., Passerat-Palmbach, J., et al. (2018). The developing human connectome project: A minimal processing pipeline for neonatal cortical surface reconstruction. *Neuroimage* 173, 88–112. <https://doi.org/10.1016/j.neuroimage.2018.01.054>.
- Manjón, J.V., Coupé, P., Martí-Bonmatí, L., Collins, D.L., and Robles, M. (2010). Adaptive non-local means denoising of MR images with spatially varying noise levels. *J. Magn. Reson. Imaging* 31, 192–203. <https://doi.org/10.1002/jmri.22003>.
- Marín, O. (2016). Developmental timing and critical windows for the treatment of psychiatric disorders. *Nat. Med.* 22, 1229–1238. <https://doi.org/10.1038/nm.4225>.
- Mathur, A.M., Neil, J.J., and Inder, T.E. (2010). Understanding brain injury and neurodevelopmental disabilities in the preterm infant: the evolving role of advanced magnetic resonance imaging. *Semin. Perinatol.* 34, 57–66. <https://doi.org/10.1053/j.semper.2009.10.006>.
- Miller, D.J., Duka, T., Stimpson, C.D., Schapiro, S.J., Baze, W.B., McArthur, M.J., Fobbs, A.J., Sousa, A.M.M., Šestan, N., Wildman, D.E., et al. (2012). Prolonged myelination in human neocortical evolution. *Proc. Natl. Acad. Sci. USA* 109, 16480–16485. <https://doi.org/10.1073/pnas.1117943109>.
- Mukherjee, P., Miller, J.H., Shimony, J.S., Conturo, T.E., Lee, B.C., Almli, C.R., and McKinstry, R.C. (2001). Normal brain maturation during childhood: developmental trends characterized with diffusion-tensor MR imaging. *Radiology* 221, 349–358. <https://doi.org/10.1148/radiol.2212001702>.
- Mukherjee, P., Miller, J.H., Shimony, J.S., Philip, J.V., Nehra, D., Snyder, A.Z., Conturo, T.E., Neil, J.J., and McKinstry, R.C. (2002). Diffusion-tensor MR

imaging of gray and white matter development during normal human brain maturation. *AJNR Am. J. Neuroradiol.* 23, 1445–1456.

Nadarajah, B., and Parnavelas, J.G. (2002). Modes of neuronal migration in the developing cerebral cortex. *Nat. Rev. Neurosci.* 3, 423–432. <https://doi.org/10.1038/nm845>.

O'Muirheartaigh, J., Robinson, E.C., Pietsch, M., Wolfers, T., Aljabar, P., Grande, L.C., Teixeira, R.P.A.G., Bozek, J., Schuh, A., Makropoulos, A., et al. (2020). Modelling brain development to detect white matter injury in term and preterm born neonates. *Brain* 143, 467–479. <https://doi.org/10.1093/brain/awz412>.

Ben-Hur, A., Elisseeff, A., and Guyon, I. (2002). A stability based method for discovering structure in clustered data. *Pac. Symp. Biocomput.* 7, 6–17.

Paredes, M.F., James, D., Gil-Perotin, S., Kim, H., Cotter, J.A., Ng, C., Sandoval, K., Rowitch, D.H., Xu, D., McQuillen, P.S., et al. (2016). Extensive migration of young neurons into the infant human frontal lobe. *Science* 354, Aaf7073. <https://doi.org/10.1126/science.aaf7073>.

Pittet, M.P., Vasung, L., Huppi, P.S., and Merlino, L. (2019). Newborns and pre-term infants at term equivalent age: A semi-quantitative assessment of cerebral maturity. *NeuroImage Clin.* 24, 102014. <https://doi.org/10.1016/j.nicl.2019.102014>.

Sanai, N., Nguyen, T., Ihrie, R.A., Mirzadeh, Z., Tsai, H.H., Wong, M., Gupta, N., Berger, M.S., Huang, E., Garcia-Verdugo, J.M., et al. (2011). Corridors of migrating neurons in the human brain and their decline during infancy. *Nature* 478, 382–386. <https://doi.org/10.1038/nature10487>.

Schuh, A., Makropoulos, A., Robinson, E.C., Cordero-Grande, L., Hughes, E., Hutter, J., Price, A.N., Murgasova, M., Teixeira, R.P.A.G., Tusor, N., et al. (2018). Unbiased construction of a temporally consistent morphological atlas of neonatal brain development. *bioRxiv*, 251512. <https://doi.org/10.1101/251512>.

Sotiras, A., Resnick, S.M., and Davatzikos, C. (2015). Finding imaging patterns of structural covariance via Non-Negative Matrix Factorization. *Neuroimage* 108, 1–16. <https://doi.org/10.1016/j.neuroimage.2014.11.045>.

Sotiras, A., Toledo, J.B., Gur, R.E., Gur, R.C., Satterthwaite, T.D., and Davatzikos, C. (2017). Patterns of coordinated cortical remodeling during adolescence and their associations with functional specialization and evolutionary expansion. *Proc. Natl. Acad. Sci. USA* 114, 3527–3532. <https://doi.org/10.1073/pnas.1620928114>.

Studholme, C., Kroenke, C.D., and Dighe, M. (2020). Motion corrected MRI differentiates male and female human brain growth trajectories from mid-gestation. *Nat. Commun.* 11, 3038. <https://doi.org/10.1038/s41467-020-16763-y>.

Sylvester, C.M., Myers, M.J., Perino, M.T., Kaplan, S., Kenley, J.K., Smyser, T.A., Warner, B.B., Barch, D.M., Pine, D.S., Luby, J.L., et al. (2021). Neonatal brain response to deviant auditory stimuli and relation to maternal trait anxiety. *Am. J. Psychiatry* 178, 771–778. <https://doi.org/10.1176/appi.ajp.2020.20050672>.

Tustison, N.J., and Avants, B.B. (2013). Explicit B-spline regularization in diffeomorphic image registration. *Front. Neuroinform.* 7, 39. <https://doi.org/10.3389/fninf.2013.00039>.

Vasung, L., Raguz, M., Kostovic, I., and Takahashi, E. (2017). Spatiotemporal relationship of brain pathways during human fetal development using high-angular resolution diffusion MR imaging and histology. *Front. Neurosci.* 11, 348. <https://doi.org/10.3389/fnins.2017.00348>.

Vasung, L., Abaci Turk, E., Ferradal, S.L., Sutin, J., Stout, J.N., Ahtam, B., Lin, P.Y., and Grant, P.E. (2019). Exploring early human brain development with structural and physiological neuroimaging. *Neuroimage* 187, 226–254. <https://doi.org/10.1016/j.neuroimage.2018.07.041>.

Volpe, J.J. (2009). Brain injury in premature infants: a complex amalgam of destructive and developmental disturbances. *Lancet Neurol.* 8, 110–124. [https://doi.org/10.1016/S1474-4422\(08\)70294-1](https://doi.org/10.1016/S1474-4422(08)70294-1).

von Monakow, C. (1905). *Gehirnpathologie* (Vienna: A. Hölder).

Wang, S., Ledig, C., Hajnal, J.V., Counsell, S.J., Schnabel, J.A., and Deprez, M. (2019). Quantitative assessment of myelination patterns in preterm neonates using T2-weighted MRI. *Sci. Rep.* 9, 12938. <https://doi.org/10.1038/s41598-019-49350-3>.

Widjaja, E., Geibprasert, S., Mahmoodabadi, S.Z., Blaser, S., Brown, N.E., and Shannon, P. (2010). Alteration of human fetal subplate layer and intermediate zone during normal development on MR and diffusion tensor imaging. *AJNR Am. J. Neuroradiol.* 31, 1091–1099. <https://doi.org/10.3174/ajnr.A1985>.

Wiese, S., Karus, M., and Faissner, A. (2012). Astrocytes as a source for extracellular matrix molecules and cytokines. *Front. Pharmacol.* 3, 120. <https://doi.org/10.3389/fphar.2012.00120>.

Wood, S.N. (2017). *Generalized additive models: an introduction with R* (CRC Press).

Wu, S., Joseph, A., Hammonds, A.S., Celniker, S.E., Yu, B., and Frise, E. (2016). Stability-driven nonnegative matrix factorization to interpret spatial gene expression and build local gene networks. *Proc. Natl. Acad. Sci. USA* 113, 4290–4295. <https://doi.org/10.1073/pnas.1521171113>.

Yang, Z., and Oja, E. (2010). Linear and nonlinear projective nonnegative matrix factorization. *IEEE Trans. Neural Netw.* 21, 734–749. <https://doi.org/10.1109/TNN.2010.2041361>.

Yeo, B.T., Krienen, F.M., Sepulcre, J., Sabuncu, M.R., Lashkari, D., Hollinshead, M., Roffman, J.L., Smoller, J.W., Zöllei, L., Polimeni, J.R., et al. (2011). The organization of the human cerebral cortex estimated by intrinsic functional connectivity. *J. Neurophysiol.* 106, 1125–1165. <https://doi.org/10.1152/jn.00338.2011>.

Zhang, H., Schneider, T., Wheeler-Kingshott, C.A., and Alexander, D.C. (2012a). NODDI: practical in vivo neurite orientation dispersion and density imaging of the human brain. *Neuroimage* 61, 1000–1016. <https://doi.org/10.1016/j.neuroimage.2012.03.072>.

Žunić Išasegi, I., Radoš, M., Krsnik, Ž., Radoš, M., Benjak, V., and Kostović, I. (2018). Interactive histogenesis of axonal strata and proliferative zones in the human fetal cerebral wall. *Brain Struct. Funct.* 223, 3919–3943. <https://doi.org/10.1007/s00429-018-1721-2>.

## STAR★METHODS

### KEY RESOURCES TABLE

REAGENT or RESOURCE	SOURCE	IDENTIFIER
<b>Antibodies</b>		
GFAP	Dako	RRID:AB_10013382; Cat# z0334
DCX (Doublecortin)	Santa Cruz Biotechnology	RRID:AB_10610966; Cat# sc-271390
MBP (SMI-99)	Biolegend	RRID:AB_2564741; Cat# 808401
Neurofilament Marker (pan axonal, SMI-312)	Biolegend	RRID:AB_2566782; Cat# 837904
<b>Deposited data</b>		
The Developing Human Connectome Project (dHCP)	<a href="#">Makropoulos et al. (2018)</a>	<a href="http://www.developingconnectome.org/">http://www.developingconnectome.org/</a>
Early Life Adversity, Biological Embedding (eLABE) and Risk for Developmental Precursors of Mental Disorders	<a href="#">Sylvester et al. (2021)</a>	<a href="https://eedp.wustl.edu/research/elabe-study/">https://eedp.wustl.edu/research/elabe-study/</a>
The Zagreb Collection of Human Brains	<a href="#">Hrabač et al. (2018)</a>	<a href="http://www.zagrebbraincollection.hr/index.php">http://www.zagrebbraincollection.hr/index.php</a>
Newborn White Matter Maturation Patterns (NeWMaPs)	This paper.	<a href="https://doi.org/10.5281/zenodo.6782004">https://doi.org/10.5281/zenodo.6782004</a>
Unbiased Morphological Atlas of Neonatal Brain Development (part of dHCP)	<a href="#">Schuh et al. (2018)</a>	<a href="https://gin.g-node.org/BioMedIA/dhcp-volumetric-atlas-groupwise">https://gin.g-node.org/BioMedIA/dhcp-volumetric-atlas-groupwise</a>
<b>Software and Algorithms</b>		
Non-negative Matrix Factorization (NMF)	<a href="#">Sotiras et al. (2015)</a> ; <a href="#">Yang and Oja (2010)</a>	[ <a href="https://doi.org/10.5281/zenodo.7076560">https://doi.org/10.5281/zenodo.7076560</a> ] <a href="https://github.com/asotiras/brainparts">https://github.com/asotiras/brainparts</a>
R Project for Statistical Computing	The R Foundation	RRID:SCR_001905; <a href="https://www.r-project.org/">https://www.r-project.org/</a>
Advanced Normalization Tools (ANTs)	<a href="#">Avants et al. (2011)</a>	RRID:SCR_004757; <a href="http://stnava.github.io/ANTs/">http://stnava.github.io/ANTs/</a>
FMRIB Software Library (FSL)	<a href="#">Jenkinson et al. (2012)</a>	RRID:SCR_002823; <a href="https://fsl.fmrib.ox.ac.uk/fsl/">https://fsl.fmrib.ox.ac.uk/fsl/</a>
Analysis of Functional NeuroImages (AFNI)	<a href="#">Cox (2012)</a>	RRID:SCR_005927; <a href="http://afni.nimh.nih.gov/afni/">http://afni.nimh.nih.gov/afni/</a>
Microstructure Diffusion Toolbox (MDT)	<a href="#">Harms and Roebroek (2018)</a>	<a href="https://github.com/robbert-harms/MDT">https://github.com/robbert-harms/MDT</a>
4dfp Suite		<a href="https://4dfp.readthedocs.io/">https://4dfp.readthedocs.io/</a>
M-CRIB-S	<a href="#">Adamson et al. (2020)</a>	<a href="https://github.com/DevelopmentalImagingMCRI/MCRIBS">https://github.com/DevelopmentalImagingMCRI/MCRIBS</a>
QuPath	<a href="#">Bankhead et al. (2017)</a>	RRID:SCR_018257; <a href="https://qupath.github.io/">https://qupath.github.io/</a>
MATLAB	MathWorks	RRID:SCR_001622; <a href="https://www.mathworks.com/">https://www.mathworks.com/</a>

### RESOURCE AVAILABILITY

#### Lead contact

Further information and requests for resources should be directed to and will be fulfilled by the Lead Contact, Aristeidis Sotiras ([aristeidis.sotiras@wustl.edu](mailto:aristeidis.sotiras@wustl.edu)).

#### Materials availability

This study did not generate new materials.

### Data and code availability

This paper analyzes existing, publicly available data from the dHCP dataset. These accession numbers for the datasets are listed in the [key resources table](#). In addition, processed datasets derived from the dHCP dataset have been deposited at Zenodo and are publicly available. Replication data from the eLAbE study can be made available to qualified investigators by written request through the eLAbE study investigators (<https://eedp.wustl.edu/research/elabe-study/>). This paper does not report original code. Any additional information required to reanalyze the data reported in this paper is available from the [lead contact](#) upon request.

## EXPERIMENTAL MODEL AND SUBJECT DETAILS

### The developing human connectome project

Infants were prospectively recruited as a part of the dHCP study, which is an observational cross-sectional open-science project (for details on study design, participant recruitment, and imaging methods, please refer to <http://www.developingconnectome.org>) (Makropoulos et al., 2018). The study was approved by the National Research Ethics Committee and written consent was obtained from all participating families before imaging.

### The early life adversity, biological embedding, and risk for developmental precursors of mental disorders (eLAbE) study

The eLAbE study was approved by the Human Studies Committees at Washington University (Sylvester et al., 2021). Informed consent was obtained from parents of all neonatal participants. Demographic characteristics of the newborns in the dHCP and eLAbE cohorts are provided in [Table S1](#).

### The zagreb collection of human brains

Late fetal and neonatal post-mortem human brain specimens without macroscopical and microscopical pathological changes were used in the study ( $n=8$ ; 33–48 postmenstrual age [weeks]; [Table S1](#)). Tissue is a part of the Zagreb Collection of Human Brains (Hrbač et al., 2018) obtained during regular autopsies after medically indicated, spontaneous abortions, or after the death of prematurely born or term infants at the clinical hospitals associated to the University of Zagreb, School of Medicine. None of the specimens exhibited evidence of ischemic brain injury. Tissue sampling was done in agreement with the Declaration of Helsinki (fifth revision, 2000), approved by the Institutional Review Board (IRB) of the Ethical Committee at the University of Zagreb, School of Medicine.

## METHOD DETAILS

### $T_1$ w and $T_2$ w MRI acquisition

366 participants had complete  $T_1$ w and  $T_2$ w datasets (dHCP 2.0 release; 2019). Fourteen infants with poor structural image quality data, incidental findings with potential clinical significance and/or impact on image analysis were excluded from the study ( $n=342$ ; age at scan: 35–44.5 weeks postmenstrual age; [Table S1](#)). All MR images were acquired using a 3T Philips Achieva scanner and a dedicated 32-channel neonatal head coil (Hughes et al., 2017). 2D sagittal and axial turbo spin echo (TSE) sequences were used to acquire both  $T_1$ w and  $T_2$ w images (all with two overlapping stacks of slices with in-plane resolution:  $0.8 \times 0.8$ ; slice-thickness: 1.6 mm resolution). Finally, by combining previously described motion correction and super-resolution reconstruction approaches (Cordero-Grande et al., 2018; Kuklisova-Murgasova et al., 2012), the images were reconstructed at  $0.5 \times 0.5 \times 0.5$  mm (Makropoulos et al., 2018).

### $T_2$ w/ $T_1$ w map generation, preprocessing, and registration

For an overview of image preprocessing and registration please refer to the [Figure S7](#). The dHCP Neonatal Structural Pipeline has been described in detail elsewhere (Makropoulos et al., 2018). After brain extraction,  $T_2$ w-brain images were further segmented into different brain tissues (9 labels including: white matter, cortical gray matter, ventricles) using the Draw-EM algorithm (of note, the white matter label does not include the internal capsule) (Makropoulos et al., 2014). Bias field corrected  $T_2$ w and  $T_1$ w images were used for further analysis. To generate  $T_2$ w/ $T_1$ w maps, the  $T_2$ w images were divided by the  $T_1$ w images for each individual using *fslmaths* (part of FSL (Jenkinson et al., 2012)).

### Neurodevelopmentally-informed nonlinear registration of the cerebral white matter

To preserve the laminar organization of the white matter, we devised a tailored non-linear registration strategy that maintains the underlying white matter topology as a function of distance from the cerebral cortex and the ventricles ([Figure S7](#)) (Huang et al., 2006). For each voxel in the white matter, distances to the (i) cortical ribbon (cortical distance map) and (ii) to the ventricles (ventricular distance map) were calculated using the *distancemap* function in FSL v6.0.0 (Jenkinson et al., 2012). These maps complement each other and are more informative at lower values (e.g., closer to the ventricle for the ventricular distance map). Therefore, for both cortical distance and ventricular distance maps all values above 6 mm were set to 6 mm.  $T_2$ w images, cortical, and ventricular distance maps were used to create age-specific templates using the “antsMultivariateTemplateConstruction2.sh” script (part of Advanced Normalization Tools [ANTs] repository) (Avants et al., 2011; Tustison and Avants, 2013). This process was repeated for each age group (one template for each week from 35–44wk postmenstrual age). A template-of-templates was generated by applying

the same process to the age-specific weekly templates. All templates are publicly available (Zenodo: <https://doi.org/10.5281/zenodo.6782004>). The linear and nonlinear transformation files were used to warp images from the native space ( $T_2w/T_1w$  ratio and white matter mask) to the template space.

To ensure that similar NeWMaPs emerge regardless of the registration approach, we registered  $T_2w$  images to the common template via previously generated weekly templates (available from the dHCP, <https://gin.g-node.org/BioMedIA/dhcp-volumetric-atlas-groupwise>) (Schuh et al., 2018) and without using distance maps (i.e., distance to cortex or distance to ventricle). All nonlinear registrations were performed with the “antsRegistrationSyN.sh” script (part of ANTs).

### Preparation for voxel-based analysis

To account for residual registration errors, a common white matter mask for voxel-wise analyses was defined as the white matter voxels that were present in more than 90% of the subjects. The non-white matter voxels in any given subject’s nonlinearly warped  $T_2w/T_1w$  map were filled with the mean of the surrounding white matter voxels, weighted by their closeness as determined by using a Gaussian kernel (full-width half-maximum [FWHM] = 1 mm). Finally, spatial smoothing was performed within the white matter mask using the *3dBlurInMask* function (FWHM = 1 mm; part of AFNI v19.2 (Cox, 2012)).

### Diffusion-weighted MRI and NODDI

Multi-shell diffusion-weighted MR images were collected as a part of dHCP study (Bastiani et al., 2019). Spin-echo echoplanar images were acquired with four different phase encoding directions (Left to Right, Right to Left, Posterior to Anterior, and Anterior to Posterior) and 3 different b-value shells (400, 1000 and 2600 s/mm<sup>2</sup>; Resolution: 1.5 × 1.5 × 3 mm<sup>3</sup>, slice overlap: 1.5 mm). A total of 300 volumes were collected with 20  $b_0$  images and 64, 88 and 128 unique directions per b-value shell. FSL EDDY was used to correct for motion, motion-induced signal drop-out, and eddy currents (Andersson and Sotiropoulos, 2016). Mean absolute motion during diffusion-weighted imaging was used as a proxy measure for in-scanner motion.

NODDI is a simplified biophysical model that characterizes microstructural tissue contributions to diffusion signal in each voxel into with 3 compartments: intracellular (within neurites), extra-cellular, and free-water compartments (Zhang et al., 2012a). Three main parameters can be derived from this model: 1) free-water isotropic volume fraction; 2) neurite density index, describing intraneurite volume fraction in a given voxel, adjusted for free water (ranging from 0 to 1); 3) the orientation dispersion index (ODI), which characterizes the orientational configuration of neurites in a given voxel (ranging from 0 [highly coherent] to 1 [highly dispersed]). The Microstructure Diffusion Toolbox (MDT v1.2.4; <https://github.com/robbert-harms/MDT>) was employed for GPU-accelerated fitting of the NODDI model (Harms and Roebroek, 2018; Harms et al., 2017). NeWMaP masks were transformed into the diffusion space via inverted nonlinear warp fields from the template space to the individual  $T_2w$  space and affine transformation matrix from  $T_2w$  space to diffusion space. We applied the resulting NeWMaP masks in the diffusion space to individual free water, neurite density, and orientation dispersion maps to extract mean values (using the *fsstats* function in FSL).

### MRI acquisition and image analysis in the eLAbE study

Participants were scanned within the first month of life during natural sleep without the use of sedating medications on a Siemens 3T Prisma scanner with a 64-channel head coil. High-resolution 3D  $T_1w$  magnetization-prepared rapid gradient-echo imaging (MPRAGE; TR=2400ms, TE=2.22ms, 0.8mm isotropic) and 3D  $T_2w$  sampling perfection with application-optimized contrasts using different flip-angle evolutions (SPACE; TR=3200 or 4500ms, TE=563ms, 0.8mm isotropic) images were acquired. Of the 311 participants that had complete  $T_1w$  and  $T_2w$  datasets, 72 infants with poor structural image quality data, incidental findings with potential clinical significance and/or impact on image analysis were excluded from the study (n=239; Table S1).

$T_1w$  and  $T_2w$  images underwent correction for gradient nonlinearity-induced and readout distortions (Glasser et al., 2013). The images were then realigned to approximate the MNI152 template orientation (using the *fsorient2std* script in FSL (Jenkinson et al., 2012)) and denoised (using the *DenoiseImage* (Manjón et al., 2010) function in ANTs). The resulting  $T_1w$  and  $T_2w$  images were coregistered using the *img\_reg\_4dnp* function (<https://4dnp.readthedocs.io/>). The Melbourne Children’s Regional Infant Brain atlas Surface (M-CRIB-S) segmentation and surface extraction toolkit was used to generate automated tissue labeling (including white matter, cortical gray matter, and ventricles) (Adamson et al., 2020). Finally, the same template creation and nonlinear registration steps that were carried out for the dHCP study were applied to the eLAbE images.

### Histological analysis

Brain tissue was fixed in 4% paraformaldehyde in 0.1M, PBS, pH 7.4, embedded in paraffin, and cut at 20μm thick sections. The coronal sections used in this study were stained by PAS-Alcian blue staining. For Nissl (Cresyl violet) staining, slides were deparaffinized in Xylene and alcohol, incubated in Cresyl Violet stain solution (0.5%), rinsed in water, dehydrated, mounted and coverslipped (Polymount). Immunohistochemistry was performed after deparaffinization of the 20μm thick sections in series of alcohol, 0.3% hydrogen peroxide treatment, and incubation in blocking solution (3% bovine serum albumin, 0.5% Triton x-100, Sigma, St. Louis, MO, USA) in 0.1M PBS, for an hour. Subsequently, sections were incubated with primary antibodies (anti-GFAP, Dako, z-0334, 1:1000; anti-DCX [Doublecortin], Santa Cruz Biotechnology, sc-271390, 1:50; SMI-99 [anti-myelin basic protein], Biolegend, 808401, 1:1000; anti-SMI-312 [panaxonal anti-neurofilament marker], Biolegend, 837904, 1:1000) overnight at room temperature, and following washes, appropriate secondary biotinylated antibodies were applied (Vectastain ABC kit, Vector Laboratories, Burlingame, CA, USA). The sections were developed with 3,3-diaminobenzidine (DAB) with a metal enhancer (Sigma, St. Louis, MO) and

coverslipped with Histomount mounting medium (National Diagnostics, Charlotte, NC). All stained slides were imaged using a high-resolution digital slide scanner NanoZoomer 2.0RS (Hamamatsu, Japan). QuPath v0.2.3. was used for visualization of whole-slide images and stain separation with color deconvolution (Bankhead et al., 2017). The thickness of the Alcian-blue<sup>+</sup> band underneath the cortical ribbon was measured perpendicular to the overlying cortex for each gyrus and sulcus at the gyral crests and sulcal fundi, respectively.

## QUANTIFICATION AND STATISTICAL ANALYSIS

### Non-negative matrix factorization

We used non-negative matrix factorization (NMF) to identify patterns where white matter  $T_2w/T_1w$  ratio covaried consistently across participants. NMF takes as input a tall non-negative data matrix  $\mathbf{X}$  (constructed by arraying column-wise vectorized aligned white matter  $T_2w/T_1w$  ratio maps,  $\mathbf{X} = [\mathbf{x}_1, \dots, \mathbf{x}_N]$ ,  $\mathbf{x}_i \in \mathbb{R}_+^D$ , where  $D$  is the number of voxels and  $N$  is the number of samples) and approximates it as a product of two non-negative matrices  $\mathbf{W}$  and  $\mathbf{H}$  ( $\mathbf{X} \approx \mathbf{WH}$ ,  $\mathbf{W} \geq 0$ ,  $\mathbf{H} \geq 0$ ; see Figure 2A for a schematic overview of the NMF procedure). The matrix  $\mathbf{W}$  ( $\mathbf{W} = [\mathbf{w}_1, \dots, \mathbf{w}_K]$ ,  $\mathbf{w}_i \in \mathbb{R}_+^D$ ) contains in each column one of  $K$  estimated patterns, where  $K$  is the user-specified number of patterns. The matrix  $\mathbf{W}$  is estimated by positively weighting variables of the data matrix that co-vary in a consistent way across the population and the weight of each variable denotes its relative contribution to the pattern. The matrix  $\mathbf{H}$  ( $\mathbf{H}^T = [\mathbf{h}_1, \dots, \mathbf{h}_K]$ ,  $\mathbf{h}_i \in \mathbb{R}_+^N$ ) contains subject-specific coefficients for each pattern, which indicate the contribution of each pattern in reconstructing the original  $T_2w/T_1w$  map. Code for NMF (<https://github.com/asotiras/brainparts>) adopts orthonormality constraints for the estimated covariation patterns ( $\mathbf{W}^T \mathbf{W} = \mathbf{I}$ , where  $\mathbf{I}$  is the identity matrix) and projective constraints for their respective participant-specific coefficients ( $\mathbf{H} = \mathbf{W}^T \mathbf{X}$ ) (Sotiras et al., 2015; Yang and Oja, 2010). Additional details regarding the implementation of NMF have been presented elsewhere (Sotiras et al., 2015, 2017).

A key difference between NMF and more commonly used methods, such as Principal Component Analysis (PCA) and Independent Component Analysis (ICA), is the non-negativity constraints on the estimated matrices  $\mathbf{W}$  and  $\mathbf{H}$ . Non-negativity constraints have been shown to lead to a parts-based representation (Lee and Seung, 1999), where parts are combined in an additive way to form a whole. This representation yields patterns that enjoy improved statistical power compared with standard mass univariate analyses and are more interpretable and reproducible compared to patterns produced by PCA and ICA (Lee and Seung, 1999; Sotiras et al., 2015).

Consistent with prior studies using this technique (Sotiras et al., 2015, 2017), we ran multiple NMF solutions requesting 2–20 patterns to obtain a range of possible solutions for comparison. We performed a split-half reproducibility analysis with bootstrapping (with replacement) to examine the stability of NMF solutions at multiple resolutions (Ben-Hur et al., 2002; Lange et al., 2004; Yeo et al., 2011). The optimal number of patterns was selected based on the stability of the results across the bootstraps, using the following criteria: i) Reproducibility: the solution with the highest mean Adjusted Rand Index (ARI) (Hubert and Arabie, 1985) across 10 split-half bootstraps; ii) Reliability (i.e., stability of the ARI across the bootstraps): the solution with the lowest standard deviation of ARI across the bootstraps. F-tests were performed to compare ARI variance between solutions. ARI provides a measure for set similarity that is adjusted for chance (Hubert and Arabie, 1985). This allows for a more balanced comparison between sets of regions when these regions vary in number. An ARI over 0.75 is deemed excellent (Fleiss et al., 2013). In addition, we calculated the reconstruction error for each solution as the Frobenius norm between the data matrix and the NMF approximation and plotted the reconstruction error for all solutions (Figure S1B).

To evaluate the robustness of our solution to different processing parameters as well as its reproducibility in a different dataset, we performed head-to-head comparisons of individual patterns from two sets of NMF results of the same size. Specifically, we compared the dHCP ( $K=9$ ) solution to (i) NeWMaPs derived using alternative preprocessing (i.e., registration approaches and application of smoothing); and (ii) NeWMaPs derived from eLAbE. We used cosine similarity (ranging from 0 [no overlap] to 1 [complete overlap]) to quantify the similarity between each pair of independently estimated patterns.

### Statistical analysis

All region-of-interest statistical analyses were performed using R v3.6.2 (<http://www.r-project.org/>). NMF masks were generated by assigning any given voxel across the white matter to the NMF pattern with the highest loading. NMF masks were registered to the  $T_2w/T_1w$  ratio maps from the eLAbE study and the native diffusion space from the dHCP study. For each NeWMaP, mean  $T_2w/T_1w$  (both dHCP and eLAbE study), free water, neurite density, orientation dispersion values were extracted for each subject using *fs/Stats* (part of FSL). To model potentially nonlinear effects of postmenstrual age on white matter  $T_2w/T_1w$  signal ratio, generalized additive models (GAMs) were fit using restricted maximum likelihood (REML, as implemented in *mgcv* package (Wood, 2017)), which produces unbiased estimates of variance and covariance parameters. To characterize potential effects of nuisance variables on the NeWMaP  $T_2w/T_1w$  ratios, we extended the GAMs by including either the head circumference or in-scanner motion (in separate models). Leave-one-out cross validation was performed to determine the utility  $T_2w/T_1w$  signal ratio extracted from the NeWMaPs in predicting newborn postmenstrual age. Generalized linear models were used to assess interaction effects (i.e., sex by age interaction effects) and contribution of NODDI parameters (free water, neurite density, and orientation dispersion index) on  $T_2w/T_1w$  signal ratio. We corrected for multiple testing using Bonferroni correction (based on  $\alpha = 0.05$  divided by the number of NeWMaPs [9];  $p < 0.0056$ ).